THE ARECIBO OBSERVATORY AS AN INSTRUMENT FOR INVESTIGATING ORBITAL DEBRIS

by

JAMES ISAIAH MURRAY

DISSERTATION

Submitted in partial fulfillment of the requirements
for the degree Doctor of Philosophy at
The University of Texas at Arlington
December, 2021

Arlington, Texas

Supervising Committee:

Fredrick Jenet, Supervising Professor
Teviet Creighton
Ramon Lopez
Zdzislaw Musielak
Yue Deng

ACKNOWLEDGEMENTS

I want to acknowledge the efforts of my dissertation committee without which I would not have been able to complete this dissertation: Dr. Fredrick Jenet, Dr. Ramon Lopez, Dr. Teviet Creighton, Dr. Zdzislaw Musielak, and Dr. Yue Deng. A special thanks to Dr. Fredrick Jenet whom has been my advisor for nearly a decade, since I was an undergraduate, over the course of many research projects. The opportunities afforded to me were instrumental in my academic career and toward the culmination of this dissertation. I would like to acknowledge the University of Texas Rio Grande Valley's Center for Advanced Radio Astronomy (CARA) for many years of support and funding for the research contained herein. The multitude of projects I worked on within CARA laid a solid framework of understanding of radio frequency instrumentation and a familiarity with the Arecibo Observatory which were crucial in the development of this work. Thank you to all the faculty, staff, and students with which I worked during my time with CARA. Thank you to Dana Whitlow and Anthony Ford for extensive guidance on the capabilities of the Arecibo Observatory which were crucial to this work. I want to acknowledge the NASA Orbital Debris Program Office (ODPO) for giving me a deep understanding of orbital debris and providing experience at the cutting edge of the field. Working with Tim Kennedy, Mark Matney, and Gene Stansbury has deepened my knowledge of radar measurements of debris immensely, and for this I am grateful. Thank you to Phillip Anz-Meador for being an infinite repository of orbital debris knowledge on which I can always count. I also want to thank Heather Cowardin and Alyssa Manis for their guidance on handling working in ODPO while completing a dissertation. Finally, a very special thanks to Melissa Ward for all her help towards the completion of this dissertation. I know I can always depend on her.

LIST OF FIGURES

LIST OF TABLES

ABSTRACT

The Arecibo Observatory as an

Instrument for Investigating

Orbital Debris

James Isaiah Murray, Ph.D.

The University of Texas at Arlington, 2021

Supervising Professor: Fredrick Jenet

In this dissertation, the Arecibo Observatory, both past and future, as an instrument for investigating orbital debris is investigated. For over three decades, models of the orbital debris environment in low Earth orbit (LEO) have been developed to assess the risk posed by orbital debris to spacecraft. While terrestrial radar measures debris 3 mm and larger and *in-situ* measurements provide data for debris smaller than 1 mm, no good data sources exist for debris between 1 mm and 3 mm in size. This results in large variations between competing orbital debris models. It also happens to be the size regime which poses the highest mission-ending risk to spacecraft. To evaluate the efficacy of the Arecibo Observatory for orbital debris measurements, new methods for evaluating the efficacy of bistatic radars for orbital debris measurements were developed. These include a new tool for calculating the lateral surface area of a bistatic radar, a method to calculate a minimum detectable debris size, and an algorithm to estimate a sensitivity-limited total count rate of debris for an observation. Each of these were validated by comparisons to debris data collected by the Haystack Ultrawideband Satellite Imaging Radar (HUSIR), the primary orbital debris radar used by NASA. Using these validated methods, the performance of

the Legacy Arecibo Telescope (LAT) and the Next Generation Arecibo Telescope (NGAT) for orbital debris measurements is estimated. It is then shown that, with appropriate hardware upgrades, it would be possible to achieve a minimum detectable debris size as small as 1 mm. These capabilities would allow data from Arecibo to significantly improve short-term debris environment models which are used to inform spacecraft design and operations, particularly for orbital debris smaller than 3 mm, which pose the highest penetration risk to most spacecraft.

TABLE OF CONTENTS

CHAPTER ONE:

INTRODUCTION

The Orbital Debris Problem

Orbital debris, also called space debris, is any man-made object in orbit around the Earth which no longer serves a useful purpose. Examples of orbital debris include the spent upper stages of launch vehicles, spacecraft which have reached the end of their useful lifespan, hardware released intentionally during spacecraft separation or operation, solid rocket motor effluents, fragments created as the result of explosions or catastrophic collisions, and paint flecks and other degradation debris released by thermal stress or small particle impacts. Orbital lifetimes of debris vary greatly, largely depending on altitude. While debris below 200 km will typically re-enter the atmosphere within a few days, debris between 200 km and 600 km take several years to fall back to Earth. At 800 km, orbital lifetimes are measured in centuries, while above 1000 km it can take more than a millennium for debris to re-enter (Orbital Debris Program Office, 2021a).

With the launch of Sputnik 1 in October 1957, the first objects to become orbital debris entered low Earth orbit (LEO). Now there are more than 23,000 tracked objects greater than 10 cm in diameter, approximately 500,000 objects between 1 cm and 10 cm, and over 100 million objects less than 1 cm in earth orbit (Liou J.-C. , 2020). Figure 1 shows a pair of computer-generated images of objects in Earth orbit currently being tracked, as of 1 January 2019, from a LEO and geostationary orbit (GEO) perspective. Approximately 95% of the objects shown are orbital debris, not functional satellites.

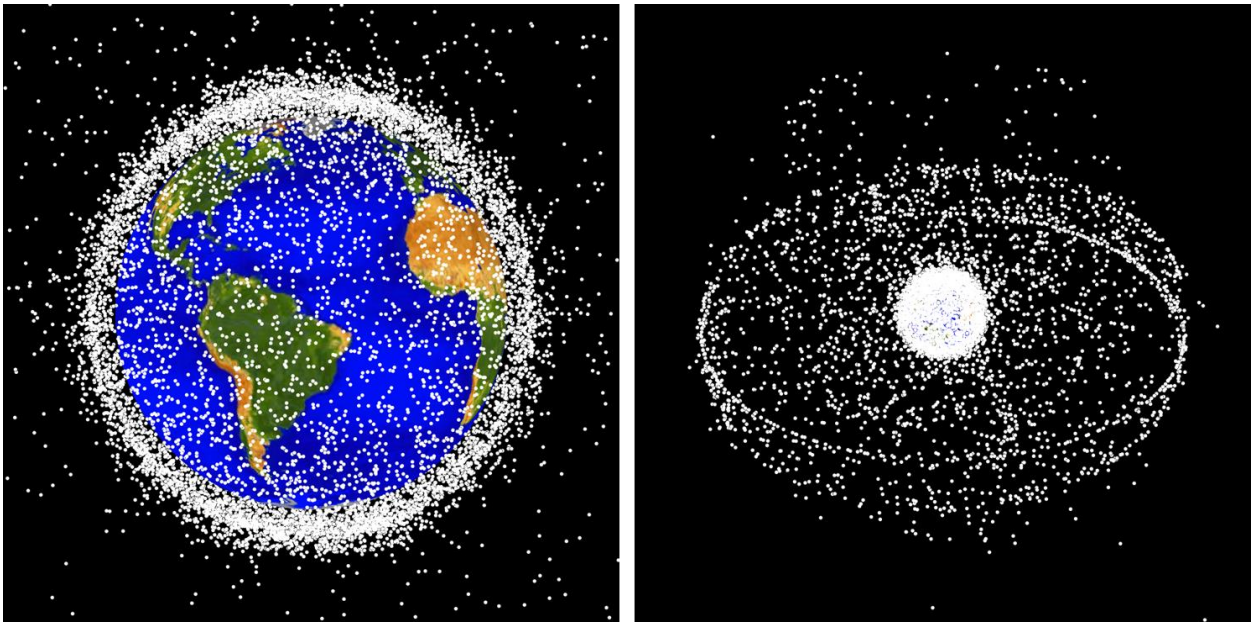

Figure 1. Illustration of tracked objects in Earth orbit as of 1 January 2019. Approximately 95% of the objects shown are orbital debris, not functional satellites. (Orbital Debris Program Office, 2021d)

The four main categories of orbital debris are rocket bodies, nonfunctional spacecraft, mission-related debris, and fragmentation debris. Figure 2 shows the cataloged population of debris in Earth orbit broken into these categories from 1 January 1956 to 1 January 2021. The number of mission-related debris and rocket bodies have been growing steadily since 1957. The number of spacecraft also exhibited a steady growth until recent years, in which a marked increase related to the rise of mega-constellations can be seen (European Space Agency, 2021). Even with the accelerated growth of spacecraft category, largest and most volatile contributor to the number of objects on orbit is still fragmentation debris. In particular, the number of objects nearly doubled from just two events; the anti-satellite (ASAT) test performed against the Fengyun-1C weather satellite by the People's Republic of China in 2007 and the accidental collision between the derelict Russian communications satellite (Cosmos 2251) and the active US commercial communications satellite (Iridium 33).

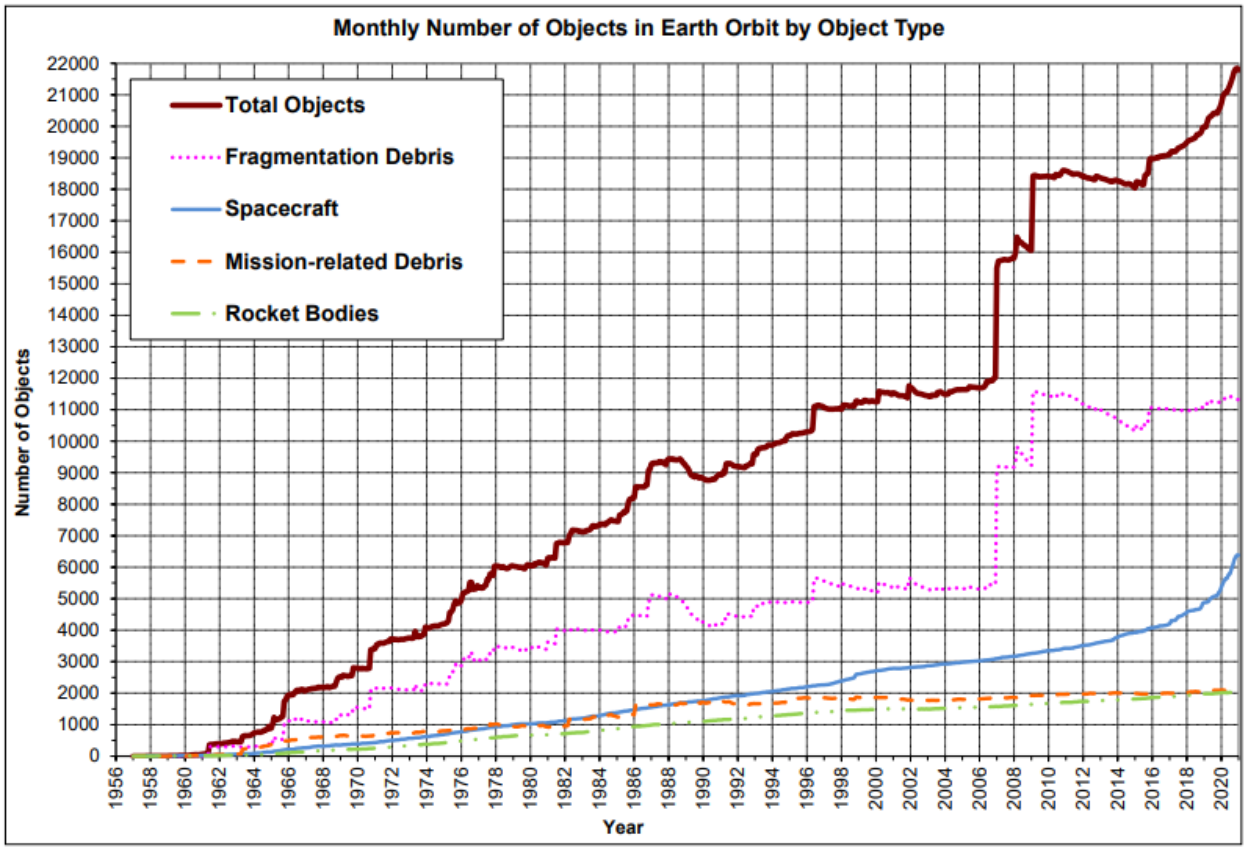

Figure 2. Monthly Number of Cataloged Objects in Earth Orbit by Object Type as of 5 January 2021. This chart displays a summary of all objects in Earth orbit officially cataloged by the U.S. Space Surveillance Network. "Fragmentation debris" includes satellite breakup debris and anomalous event debris, while "mission-related debris" includes all objects dispensed, separated, or released as part of the planned mission. (Orbital Debris Program Office, 2021b)

Although the Iridium-Cosmos collision was the first accidental collision between two intact objects, it was not the first accidental collision on orbit. There have been five additional confirmed accidental collisions resulting in a catastrophic satellite breakup; Cosmos 1934 in 1991, Cerise in 1996, DMSP 5B F5 R/B in 2005, Sentinel 1A in 2016, and Yunhai 1-02 in 2021 (Anz-Meador, Opiela, Shoots, & Liou, 2018) (Space-Track, 2021). With the exception of Sentinel 1A, which collided with a micrometeoroid, each of the satellites collided with a piece of orbital debris. In 1978 Donald Kessler wrote one of the first papers presenting the risk of the creation a debris belt around the Earth through collisional fragmentation events (Kesseler & Cour-Palais, 1978). With few environmental sinks, each fragmentation event increases the number of objects and thus the

probability of collision between objects eventually making access to certain orbital ranges difficult for many years.

In 2008, (Liou & Johnson, 2008) showed that the debris environment has already reached a critical density after which the production rate of new breakup debris due to collision would exceed the loss of objects due to orbital decay, meaning that the number of debris objects on orbit will continue to grow, even in a "no future launches" scenario, i.e. assuming that all launches of spacecraft into orbit would cease entirely. Figure 3 shows the effective number of objects greater than 10 cm in LEO projected out to approximately 2210, as predicted by (Liou & Johnson, 2008). In this "best case" scenario, collision debris will replace other decaying debris keeping the environment steady until about 2055. After 2055 the number of fragments will continue to grow steadily, suggesting that active debris removal is a necessary step to limit the growth of the debris population in the future.

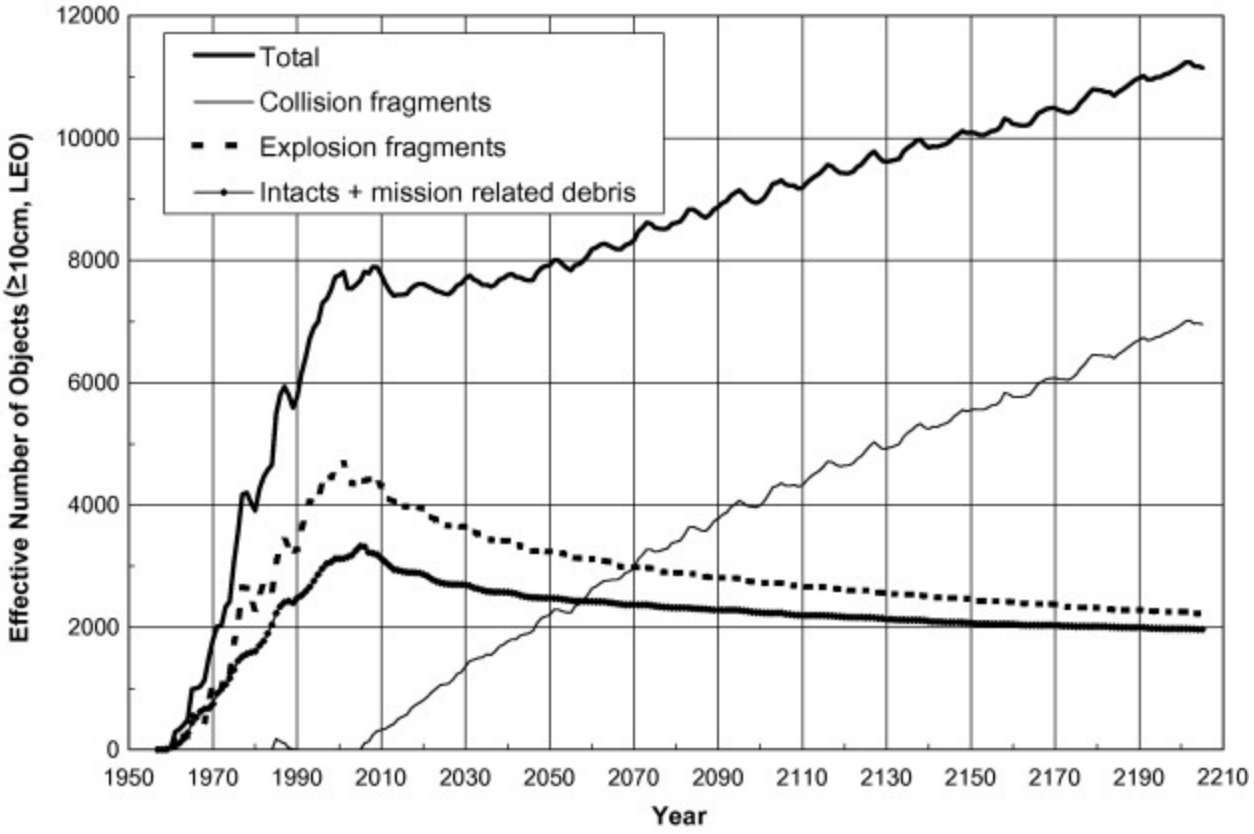

Figure 3. Growth of low Earth orbit (LEO) populations under a "no future launch" scenario. The effective number of objects is defined by the fractional time, per orbital period, an object spends in LEO. (Liou & Johnson, 2008)

Orbital Debris as a Threat

It is important to limit the growth of orbital debris because of the danger posed to spacecraft, even by small scale debris. Meteoroids and micrometeoroids are another, naturally occurring, collision risk for spacecraft originating from comets, asteroids, and ejecta from impacts on other solar system bodies. In many altitude and size regimes, the debris population has already surpassed that of the micrometeoroid background. Orbital debris is currently the predominate collision risk in LEO, with debris comprising two-thirds of the risk to the International Space Station (ISS) (Christiansen & Lear, 2012). Debris as small as 0.1 mm can penetrate a space suit, (when the shuttle program was still active) a 1 mm could damage the Space Shuttle pay-load bay and 5 mm could penetrate the Space Shuttle crew cabin (National Research Council, 1998). Figure

4 depicts damage caused to the Space Transport System (STS)-115 right-hand side radiator from a 1.2 mm debris particle impacting at approximately 9 km/s. At these speeds, even a small piece of debris can cause significant damage.

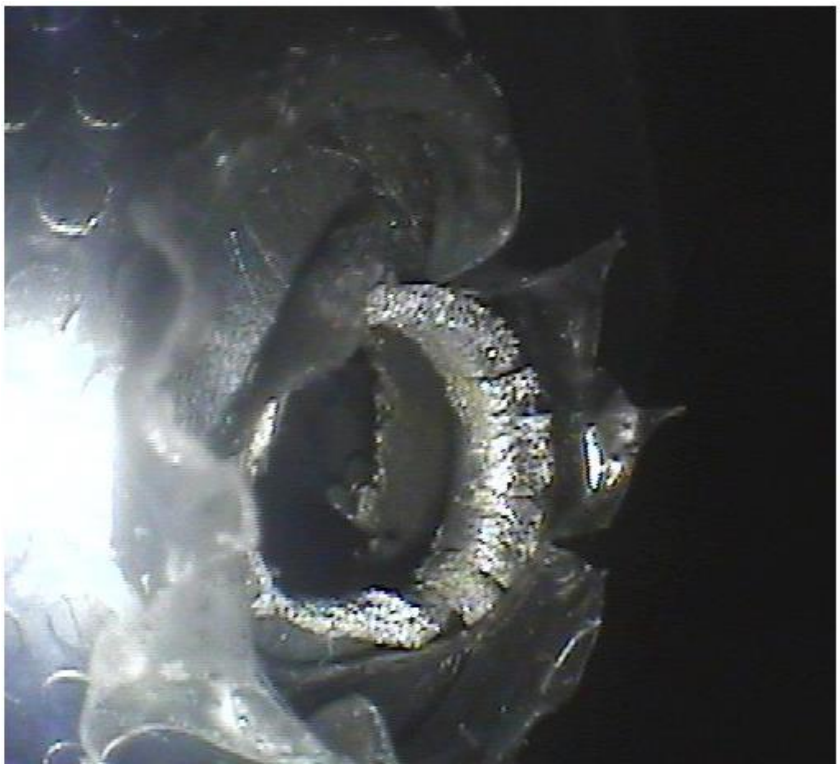

Figure 4. This is a view of the STS-115 right-hand side radiator #4 MMOD hit. Based on analysis of the entry hole residue and impact testing, the impactor was possibly a piece of electronic circuit board material. Estimated diameter of this debris particle was 1.2mm impacting at about 9 km/s. (Hyper Velocity Impact Technology, 2021)

The nominal size limit for debris that is tracked and can be avoided is 10 cm. Debris smaller than this, while still dangerous, cannot be avoided. The risk they pose must be mitigated through advanced shielding techniques, such as Whipple shields, Multi-Shock shields, and Honeycomb Panel shields, among others. Due to the orbital velocities in LEO, almost all collisions are hyper-velocity impacts, where the impact speed is faster than the speed of sound in the material. Due to the immense speed and resultant kinetic energy of such collisions, the effect is more similar to an explosion than a simple impact. Figure 5 shows the results of hyper-velocity impacts of spherical

aluminum projectiles on a monolithic aluminum target and a Whipple shield. While the impact on the monolithic target results in large cratering and a detached rear wall, the thin bumper of the Whipple shield shocks and fragments the incoming particle and dissipates the energy such that the rear wall of the shield is not penetrated. Since much of the debris that cannot be avoided can still cause significant damage, understanding the small debris environment in LEO is crucial for spacecraft design and operation.

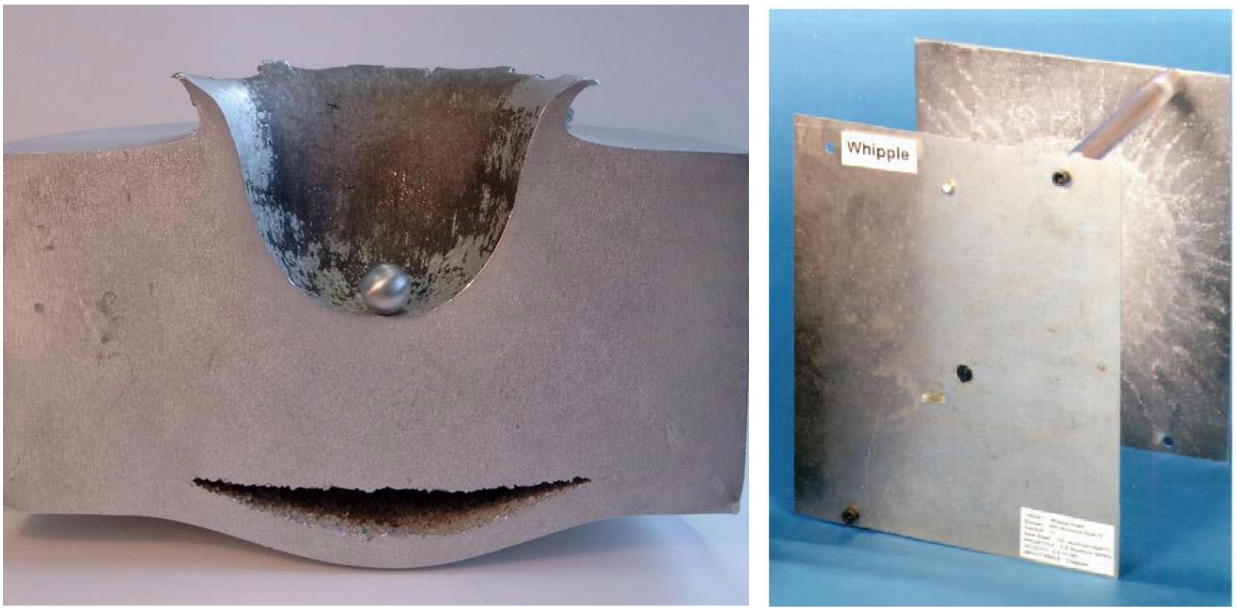

Figure 5. Results of hyper-velocity impacts of spherical aluminum projectiles on a monolithic aluminum target (left) and a Whipple Shield (right). (Christiansen & Lear, 2012)

Response to the Orbital Debris Problem

The comprehensive approach taken by the NASA ODPO to the orbital debris problem involves both laboratory and environmental measurements which form the basis of models of the environment. These models inform the development of debris mitigation practices, spacecraft design standards, and space policy development (Liou J.-C. , 2020).

Orbital Debris Environment Models

The three main types of debris environment models are short-term collisions risk assessment models, like NASA's Satellite Breakup Risk Assessment Model (SBRAM) (Matney,

2000); long-term environment evolution models, like NASA's LEO-to-GEO Environment Debris model (LEGEND) (Liou, Hall, Krisko, & Opiela, 2004); and engineering models, like NASA's Orbital Debris Engineering Model (ORDEM) (Krisko, 2014). Short-term models are used to determine the immediate risk to spacecraft caused by a recent satellite breakup. Long-term models are for assessing the efficacy of mitigation and remediation tactics. Engineering models are used to predict the flux of particles expected to be encountered over the course of the lifetime of a spacecraft's mission. It can also be used for debris measurement observation planning. An engineering model is not a design tool itself, but it is used by spacecraft design tools to inform the designer of the flux of debris the spacecraft is likely to encounter.

Orbital Debris Measurements

Measurements can be divided into two general categories: laboratory measurements and environmental measurements. Laboratory measurements include satellite breakup experiments such as NASA's Satellite Orbital debris Characterization Impact Test (SOCIT) (McKnight, Johnson, Fudge, & Maclay, 1995), which was integral to the development of NASA's Statistical Satellite Breakup Model (SSBM), and NASA's more recent DebriSat satellite breakup experiment conducted to update the SSBM for satellites using more modern spacecraft materials (Liou, et al., 2013) (Murray, et al., 2019). Radar Cross-Section (RCS) measurements performed on representative debris fragments formed the basis of the NASA radar Size Estimation Model (SEM) (Bohannon, Caampued, & Young, 1994) (Xu & Stokely, 2005). NASA's Optical Measurements Center (OMC) performs photometric and spectral measurements of spacecraft materials to characterize and model optical data acquired from ground-based telescopes (Cowardin, et al., 2014).

Environmental measurements include satellite catalog information provided by the United States Space Surveillance Network (SSN), radar measurements, optical measurements, and *in-situ*

measurements. Optical measurements using ground-based telescopes are used for statistical surveys in both LEO and GEO. Telescopes that have been used for optical measurements by NASA include a charge-coupled device (CCD) equipped 0.3 m Schmidt camera, referred to as the CCD Debris Telescope (CDT); a 3 m diameter liquid mirror telescope, the Liquid Mirror Telescope (LMT); the 0.6 m Michigan Orbital Debris Survey Telescope (MODEST); and the 1.3 m Eugene Stansbery Meter-Class Autonomous Telescope (ES-MCAT), NASA's only telescope currently actively taking debris measurements (Orbital Debris Program Office, 2021c).

Data for objects larger than 10 cm in LEO and 1 m in GEO comes from the SSN, which utilizes a network of radar and optical sensors to maintain a catalog of resident space objects. Figure 6 shows a map of the locations of the various radar and optical sensors that comprise the SSN. Due to the locations of the sensors that comprise the network, resident space objects can be tracked at all orbital inclinations.

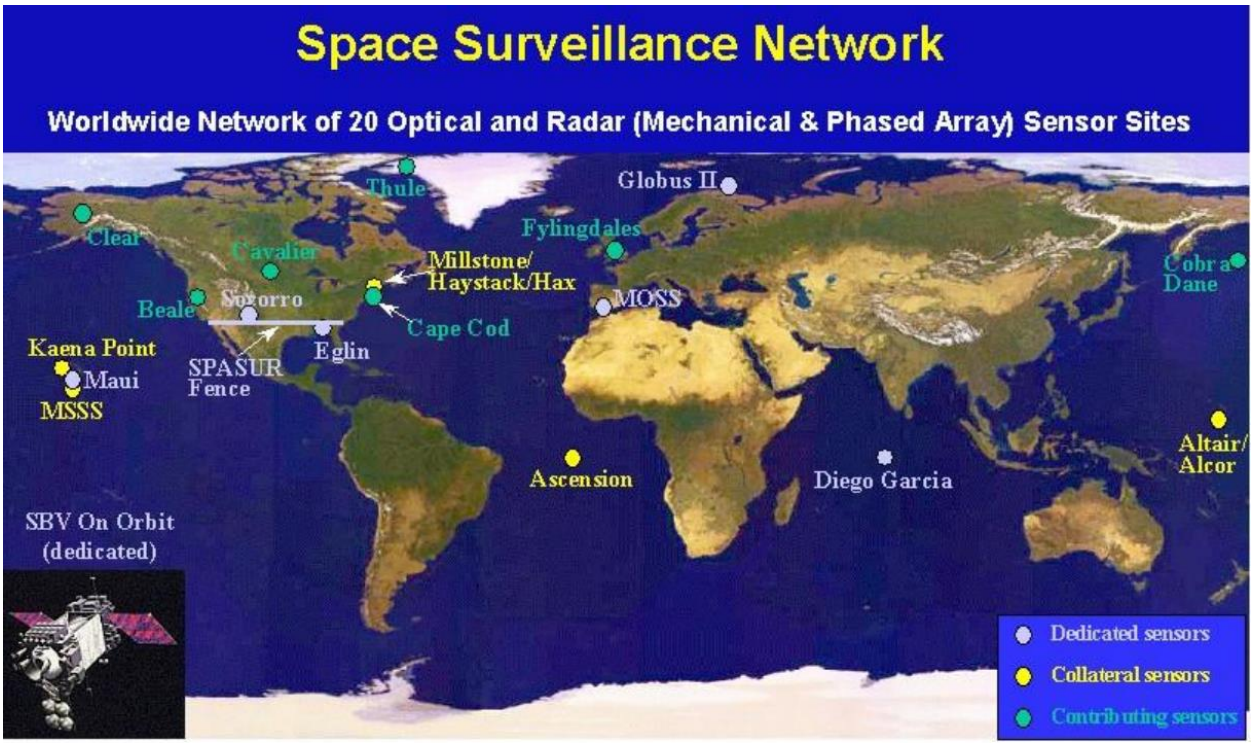

Figure 6. Locations of the various sensors comprising the United States Space Surveillance Network. (NASA, 2008)

Data for objects smaller than 1 mm comes from *in-situ* measurements, both analyzing the impact craters from returned spacecraft and dedicated *in-situ* sensors. Examples include the Long Duration Exposure Facility (LDEF), craters surveys on the Space Shuttle windows and radiators, the Hubble Space Telescope's Wide Field and Planetary Camera (WFPC2), craters in multilayer insulation (MLI) from the Hubble Space Telescope, and NASA's Space Debris Sensor (SDS) (Liou, et al., 2009) (Ward & Anz-Meador, 2019) (Anz-Meador, et al., 2019). Terrestrial radar currently provides data from 10 cm down to 3 mm in size (Vavrin, et al., 2019). The primary radar used by NASA for orbital debris measurements is the Haystack Ultrawideband Imaging Radar (HUSIR), previously the Haystack Long Range Imaging Radar (LRIR). HUSIR is operated by the Massachusetts Institute of Technology's Lincoln Laboratory (MIT/LL) and has been collecting roughly 600 hours of statistical measurements of the debris environment in LEO per year nearly continuously since the early 1990's (Stansbery, Bohannon, Pitts, Tracy, & Stanley, 1992) (Settecerri, Stansbery, & Hebert, 1999) (Foster, Stansbery, Matney, Benbrook, & Jarvis, 2003) (Stokely, Foster, Stansbery, Benbrook, & Juarez, 2006) (Horstman, Papanyan, Juarez, & Hamilton, 2014) (Murray, Blackwell, Gaynor, & Kennedy, 2019) (Murray & Kennedy, 2020) (Murray & Kennedy, 2021). HUSIR characterizes the environment for debris as small as 5.5 mm at 1000 km altitude. The NASA ODPO has also collected orbital debris measurements using the Goldstone Orbital Debris Radar (Goldstone), operated by NASA's Jet Propulsion Laboratory (JPL) since as early as 1989 and continuing today (Goldstein & Randolph, 1992) (Goldstein & Goldstein, 1995) (Goldstein, Goldstein, & Kessler, 1998) (Matney, Goldstein, Kessler, & Stansbery, 1999) (Murray, Miller, Matney, Anz-Meador, & Kennedy, 2019) (Lee, Slade, Jao, & Rodriguez-Alvarez, 2020) (Miller, Murray, & Kennedy, 2021a) (Miller, Murray, & Kennedy, 2021b). Goldstone is a bistatic radar system capable of characterizing the orbital debris

environment down to approximately 3 mm at 1000 km altitude, making it the most sensitive radar in the world currently used for orbital debris measurements in LEO.

Motivation

In-situ measurements typically provide data for orbital debris smaller than 1 mm in LEO. The most sensitive terrestrial radars used for orbital debris measurements can characterize the environment for debris down to approximately 3 mm in LEO. This leaves a gap between 1 mm and 3 mm for which there is no good source of debris data in LEO. Figure 7 depicts the notional size and altitude constraints of various data sources employed by NASA for orbital debris measurements. Also depicted in the figure are the relative orbital inclinations (in degrees) available to the radars for measurement. This is limited by the observation geometries employed by the various radars. In particular, it is important to note that the terrestrial radar data sources currently employed by NASA do not characterize debris with an orbital inclination lower than 30°.

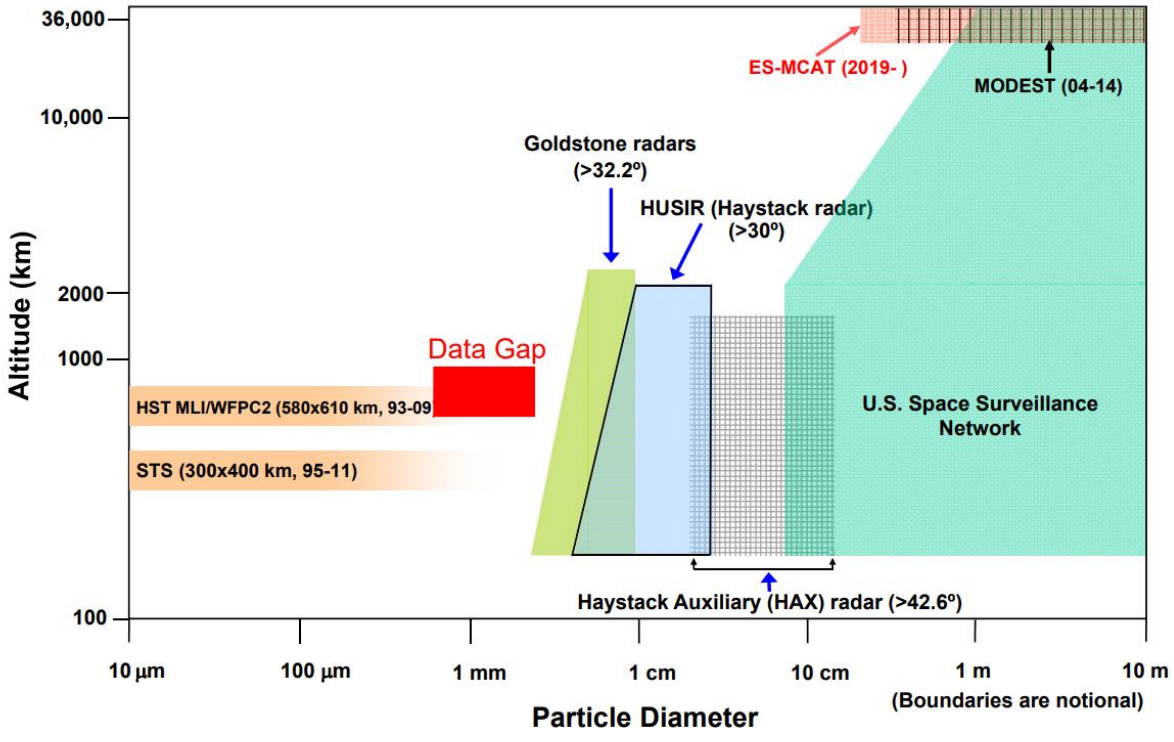

Figure 7. Notional size, altitude, and inclination constraints of various data sources employed by NASA for orbital debris measurements. (Liou J.-C. , 2020)

In 2015, NASA published the Micrometeoroid and Orbital Debris Assessment of the Joint Polar Satellite System (Squire, et al., 2015). A key finding of the report states that the greatest risk to spacecraft is posed by orbital debris in the 0.6 mm to 3 mm size regime. Additionally, the report compared the predicted debris flux using several orbital debris environment models including NASA's ORDEM 3.0, NASA's ORDEM 2000 (an older version of ORDEM), ESA's Meteoroid and Space Debris Terrestrial Environment Reference (MASTER) 2009, and the Aerospace Corporation's Aerospace Debris Environment Projection Tool (ADEPT). It was shown that the four models that were compared agreed to within a factor of approximately two for most debris sizes larger than 3 mm. However, the models disagreed significantly for debris smaller than 3 mm, which is also the size that poses the highest mission-ending risk to spacecraft. Therefore, it is of interest to find new data sources to help refine the models in this under-sampled size regime.

There are many radars and radio telescopes that could be combined to create sensitive bistatic radars that could potentially bridge the size gap. ESA has performed bistatic radar observations with its Tracking and Imaging Radar (TIRA) using the Effelsburg radio telescope as a receiver (Leushacke, Mehrholz, & Jehn, 1997) (Ruiz, Leushacke, Jehn, & Keller, 2006). This bistatic configuration reduced their minimum detectable size down to 1 cm, a significant improvement over their 2 cm monostatic limit. Goldstone is a bistatic radar that provides measurements of debris as small as 3 mm at 1000 km altitude. In 1992, NASA performed a bistatic radar experiment with the planetary radar of the Arecibo radio telescope as a proof of concept for using terrestrial radar for orbital debris measurements, during which objects as small as 5 mm were detected (Matney, Goldstein, Kessler, & Stansbery, 1999). The Arecibo observatory had several upgrades after this experiment, including an increase in transmission power, which would increase the sensitivity of the radar for orbital debris measurements. Unfortunately, due to the recent

collapse of the Arecibo dish, now referred to as the Legacy Arecibo Telescope (LAT), much of these capabilities are no longer currently available. However, the proposal for the Next Generation Arecibo Telescope (NGAT) promises improved radar performance over the already substantive legacy system (Roshi, et al., 2021). This sensitivity could be leveraged to fill in the knowledge gaps that exist in the orbital debris environment in LEO between 1 mm and 1 cm in size, while simultaneously measuring an under-sampled range of orbital inclinations.

Objective

The Arecibo Observatory had one of the largest and most sensitive radio instruments in the world, which allowed the Arecibo Observatory to push the boundaries of knowledge in astronomy, atmospheric science, and planetary science. These capabilities are not currently available due to the recent collapse of the LAT. However, the NGAT promises improved radar performance over the legacy system. Figure 8 shows the cumulative flux versus size predicted by ORDEM 3.0 with notional overlays depicting the size coverage of various ORDEM input data sets. This dissertation will show that the Arecibo Observatory could bridge the gap between the sub-millimeter *in-situ* data and the greater than 3 mm terrestrial radar data and provide validation of orbital debris environment models in the size regime which poses the highest risk of penetration to most spacecraft. To accomplish this, tools for evaluating the efficacy of a general bistatic or monostatic radar for debris observations are developed.

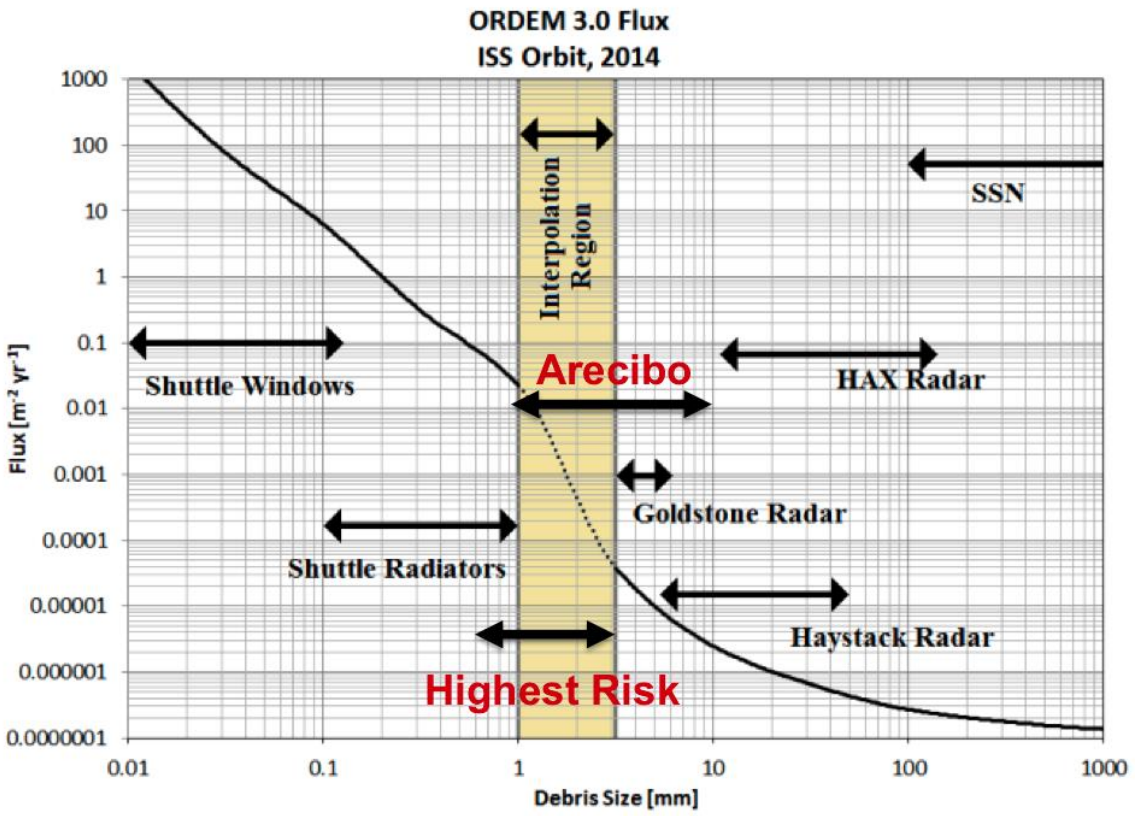

Figure 8. Cumulative flux versus size predicted by ORDEM 3.0 with notional overlay depicting the size coverage of various ORDEM input data sets and predicted NGAT performance (Squire, et al., 2015), with added overlays for emphasis.

Chapter Overview

Two key performance metrics for evaluating the utility of any configuration are the minimum detectable debris size and the total debris count rate. While the former mostly depends on the radar sensitivity, total debris count rate depends on the sensitivity, flux of debris on orbit, and lateral surface area of the sensor field of view. NASA's ORDEM can be used to predict the flux of debris passing through the line of sight of a radar or telescope. This flux is related to a count rate through the calculation of the lateral surface area of the sensor. Since the shape of the beam overlap in a bistatic radar system is complex, a method for calculating the lateral surface area of a generalized bistatic radar (which did not previously exist) is needed.

In Chapter Two, a generalized method that was developed for calculating the lateral surface area of a bistatic radar is described. Comparisons to a monostatic lateral surface area calculation algorithm are presented and shown to be in good agreement. A case study of a more recently implemented observation configuration of Goldstone (bistatic) is shown. Finally, a general guide for the relative error of the monostatic lateral surface area algorithm relative to the generalized bistatic algorithm as a function of bistatic baseline and intersection altitude is developed. This can be used to inform when the bistatic algorithm must be used, based on the error tolerance of the end user.

In Chapter Three, a method for estimating a total count rate limited by the sensitivity of the radar is presented. First, a method for estimating the minimum detectable RCS and debris size is shown. Then an overview of the modeled data from ORDEM is given. Next, a method to incorporate probability of detection into the altitude dependent ORDEM flux output is exhibited. Finally, a functional form for an altitude- and sensitivity-integrated total count rate is derived.

In Chapter Four, it is shown that the NGAT has the capability to close the size gap for debris data sources in LEO. First, an overview of the LAT and NGAT systems are presented. Then, using techniques developed in Chapter Two and Chapter Three, the detection rate and minimum detectable size estimates for the various configurations of the LAT and NGAT are presented. Next, design changes that would significantly improve the performance of the NGAT for statistical debris measurements in LEO are discussed. Finally, predictions of the expected performance increases expected from these design changes are then presented.

The dissertation is then summarized in Chapter Five and potential future work is presented. One future work topic involves developing methods to analyze existing LAT radar measurements for the presence of orbital debris signatures to characterize the low-inclination 1 cm orbital debris

population. Another topic would investigate the ability of Arecibo to perform observations of debris in GEO and cislunar orbital regimes. A third future work topic would be applying the methods developed here to other previously unexamined radar assets, such as the new Green Bank Telescope (GBT) planetary radar.

CHAPTER TWO:

BISTATIC LATERAL SURFACE AREA CALCULATION

The flux of debris passing through the line of sight of a radar or telescope can be predicted using an orbital debris engineering model, such as NASA's ORDEM. The lateral surface area of the sensor is used to relate the flux (number per unit area per unit time) to a count rate (number per unit time). For a monostatic radar this area is the conic frustum (truncated cone) surface area of a cone with angular divergence determined by using the half-power (3 dB) point of the radar (Stokely, Stansbery, & Goldstein, 2009). The cone truncation is related to the minimum and maximum slant ranges observed by the radar. The shape of the beam overlap in a bistatic radar system is more complex and a general a method for calculating the lateral surface area of a generalized bistatic radar did not exist.

A new method of calculating the lateral surface area of a generalized bistatic radar system has been developed. The new method maps the radar beam overlap in 3D space, calculating the area of the complex surface formed by the gain product of the two antennas. In this Chapter, a monostatic lateral surface area algorithm based on the beam model used by NASA is presented. Next, the newly developed bistatic method is described. Comparisons of the monostatic and new bistatic lateral surface area calculation methods for the monostatic case are presented. Then, results of a sample lateral surface area calculation for the bistatic observation configuration currently employed by Goldstone are shown. Finally, a guide for total error as a function of baseline and target altitude is established. This guide informs the user when the bistatic area calculation must be used, based on the error tolerance of the application.

Monostatic Lateral Surface Area Calculation

To calculate lateral surface area, one models the beam of the radar as a conic frustum with an opening angle equal to the half-power beamwidth (HPBW) of the radar and whose bases are perpendicular to the radar boresight. This algorithm requires the sensor position, sensor pointing direction (azimuth and elevation), sensor HPBW, and the two altitudes between which the area is to be computed i.e. the start and stop altitudes. Using the sensor location and pointing, the corresponding start and stop slant ranges (R_1 and R_2) are computed. An example of the geometry used for the calculation is shown in Figure 9. The vector $\vec{p}$ is the sensor position; $\hat{R}$ is the boresight unit vector; H_1 is the starting altitude with R_1 and $\overrightarrow{r_1}$ being the corresponding slant range and position vector; H_2, R_2, and $\overrightarrow{r_2}$ are the stopping altitude, slant range, and position vector; $\vec{r}_{avg}$ is an average of $\overrightarrow{r_1}$ and $\overrightarrow{r_2}$ used to calculate the local angle with respect to the vertical; and A is the lateral surface area of the conic frustum with opening angle θ_{HPBW}.

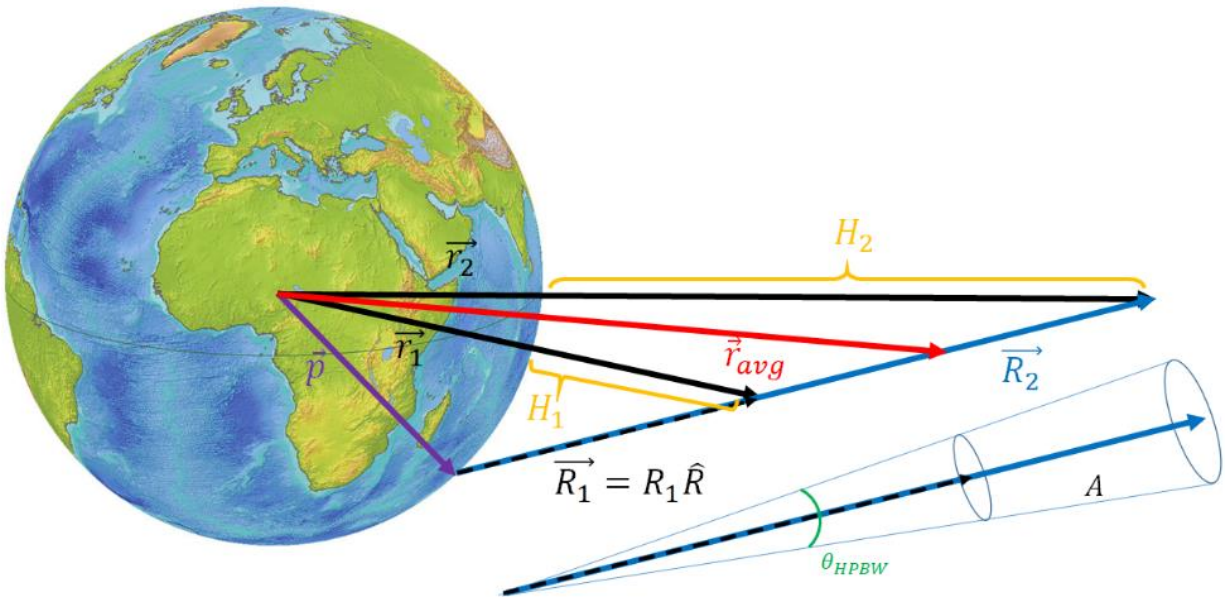

Figure 9. Geometry used for lateral surface area calculation.

The lateral surface area between these slant ranges is then calculated using equation 1, which uses a small angle approximation for the HPBW. Finally, the area is corrected by multiplying by the cosine of the local angle with respect to the vertical.

$$A = \theta_{HPBW} \frac{\pi}{2} * (R_2^2 - R_1^2), \qquad (1)$$

This calculation method is applicable to monostatic "pencil-beam" radars. It can also be applied to bistatic radars with a sufficiently short baselines, where the opening angle of the frustum defined by the 6 dB point of the product of the transmitter and receiver normalized radiation patterns (Kennedy, Murray, & Miller, 2020).

Bistatic Lateral Surface Area Calculation

In a bistatic radar, the observation volume is confined to the intersection of the transmitter beam and the receiver beam. Calculating the intersection volume is a common problem in experiments where multiple transmitters and receivers are illuminating and observing the same volume. An analytic solution for the intersection volume of intersecting cylinders has been given by (Hubbell, 1965). Analytic solutions to symmetric congruent cones have been given in (Beyer, Fawcett, Mauldin, & Swartz, 1987) and (Hughes & Clamons, 1974). Several numeric approaches were presented in (Balogun, Brunetti, & Cesareo, 2000) for calculating the intersection volume for the general intersection of two cones.

Although a similar problem, the calculation needed here is not the volume of the intersection, but area of the surface defined by the intersection of the two volumes. Additionally, the calculations need not just the total surface area, but surface area as a function of altitude because debris flux is not uniform in altitude. The approach taken involves calculating the product of the normalized gain of each antenna at discrete points in full 3D on a World Geodetic System (WGS)-84 ellipsoid. The beam intersection is taken to be the points in space for which this gain

product is greater than -6 dB, resulting in a non-trivial 6 dB surface in general. The lateral surface area between two altitudes is then calculated by approximating the surface as a series of stacked polygonal cylinders. Their individual areas are calculated as the product of its perimeter and height and summed to calculate the total area.

To calculate the lateral surface area between two slant ranges (as determined by the start and stop altitudes desired) one begins by choosing a set of N points $\{(x_i, y_i) \mid i = 0,1,\ldots,N-1\}$ on a grid in a plane perpendicular to the boresight vector of one antenna. Then for each point the angular offset from each antenna θ is calculated as

$$\theta_{i,j} = \cos^{-1}\frac{\vec{r}_{i,j} \cdot \vec{b}_j}{|\vec{r}_{i,j}||\vec{b}_j|}, \qquad (2)$$

where $\vec{r}_{i,j}$ is the vector from the j^{th} antenna to the i^{th} point in the plane and $\vec{b}_j$ is the boresight vector of the j^{th} antenna. Then the convex hull of points within the beam is taken where "in the beam" is defined as where the normalized gain product of the two antennas is greater than -6 dB, which can be represented as

$$H = ConvexHull\left((x_i, y_i)\middle|\prod_{j=1,2} G_j(\theta_{i,j}) \geq 0.25\right), \qquad (3)$$

where $G_j(\theta)$ is the normalized gain pattern of the j^{th} antenna as a function of the angular offset from boresight. Here the default model for each antenna is a uniformly illuminated circular aperture where the pattern produced is well known as an Airy disk and is given by

$$G(\theta) = \left(\frac{2J_1(ka\sin\theta)}{ka\sin\theta}\right)^2, \qquad (4)$$

where J_1 is the Bessel function of the first kind of order one, $k = \frac{2\pi}{\lambda}$ is the wave number, a is the radius of the aperture, and θ is the angular offset from the normal vector of the aperture.

Although an Airy disk has been chosen as the default, any axisymmetric beam pattern can be used. The geometry for these calculations is shown in Figure 10.

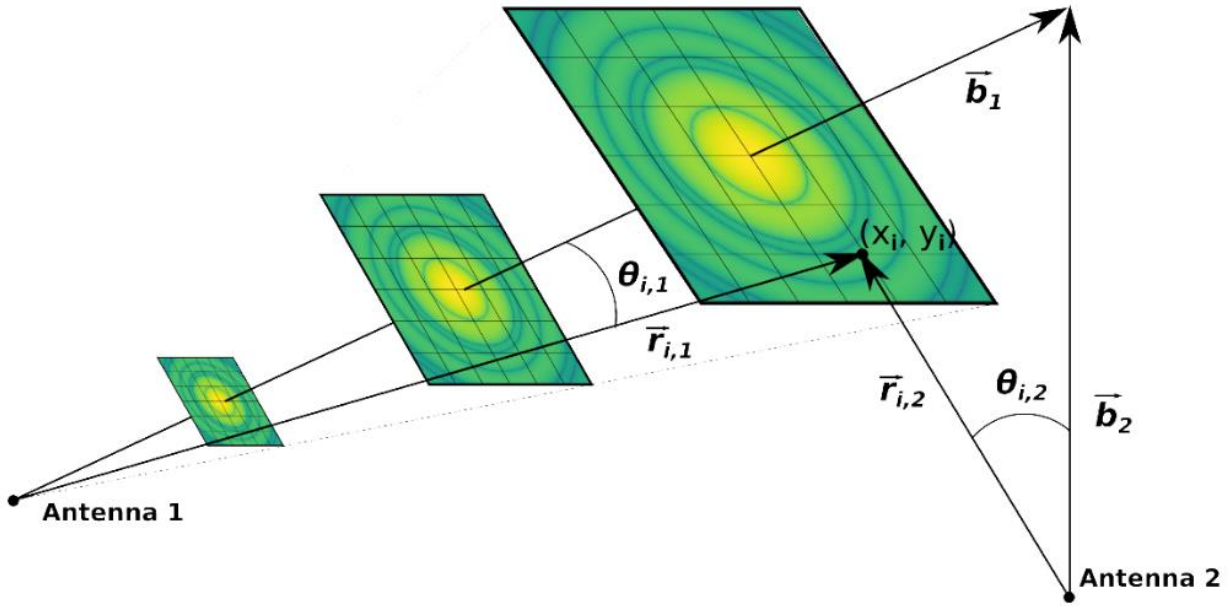

Figure 10. Geometry used for the calculation of the lateral surface area of the beam intersection.

The convex hull of a set of points is the smallest convex set that contains the points. There are many algorithms for calculating a convex hull. Here, the Qhull algorithm is used (Barber, Dobkin, & Huhdanpaa, 1996), specifically the SciPy (Virtanen, et al., 2020) implementation. In addition to returning the points comprising the convex hull, QHull returns the surface area and volume of the hull, or perimeter and area if the hull is 2D, as used in this paper.

Once the perimeter of the 6 dB surface in the plane is calculated, the lateral surface area of the beam overlap between this plane and the next is approximated as a polygonal cylinder whose lateral surface area is the product of the perimeter of its base and its height, i.e. the distance between the two planes. As shown in Figure 11, when calculating the lateral surface area between two planes, one can choose the base of the approximating cylinder to be in either the bottom or top

plane resulting in an under- or over-estimate of the true area of the surface depending on the relative values of the perimeter in each plane.

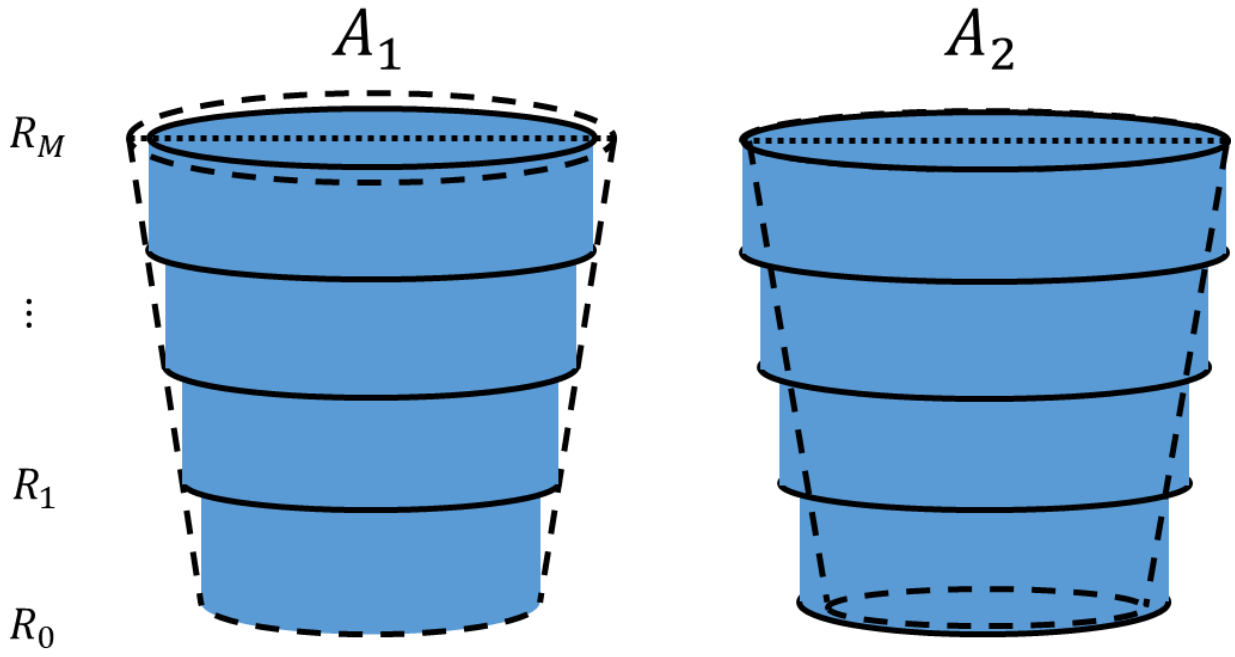

Figure 11. Examples of under- and over-estimates of lateral surface area. Here a conic frustum is used as the example 6 dB surface for simplicity.

To improve accuracy, an average of the two is taken. For an approximation using M cylinders, assuming equally spaced planes, the area is calculated as

$$A = \sum_{i=0}^{M-1} \left(P(R_i) + P(R_{i+1})\right) * \frac{R_M - R_0}{2M}, \qquad (5)$$

where $P(R_i)$ is the perimeter of the 6 dB surface in the plane at a range R_i, R_0 is the range corresponding to the start altitude, R_M is the range corresponding to the stop altitude, and M is the number of cylinders. Like in the case of the monostatic algorithm, the final area is calculated by multiplying by the cosine of the local angle with respect to the vertical. The same off-vertical area correction as the monostatic algorithm is used, instead of constructing the planes directly in altitude, to ensure compatibility. Since these off-axis corrections are based on the direction in

which the radar is pointed, it turns out the accuracy of the bistatic results, when compared to the monostatic algorithm, is independent of the pointing. This will be discussed in greater detail in the following section.

Comparison of the Monostatic Case

Although this new algorithm was developed for the generalized bistatic case, it is validated by comparing results of the monostatic algorithm to the bistatic algorithm in the monostatic case. The HUSIR radar, used extensively by the NASA ODPO, was chosen for this comparison. These comparisons were made in two common observation configurations employed by HUSIR. The first has the radar pointing at an elevation of 75° and an azimuth of 90° (eastward) which is referred to as 75E. The second has the radar pointing at an elevation of 20° and an azimuth of 180° (southward) which is referred to as 20S (Murray, Miller, Matney, & Kennedy, 2019). The relevant location and operational parameters for HUSIR are presented in Table 1.

Table 1. Relevant location and operational parameters for the HUSIR radar. Latitude, longitude, and elevation are relative to the WGS-84 Earth ellipsoid. (Murray, Blackwell, Gaynor, & Kennedy, 2019)

Latitude	42.623287° N
Longitude	288.511846° E
Elevation	115.69 m
Transmitter Frequency	10.0 GHz
Antenna Half-Power Beamwidth	0.058°
Antenna Diameter	36.6 m

As noted earlier, the default beam model used by the newly developed method is that of a uniformly illuminated aperture. When using the center frequency and antenna diameter of the HUSIR radar with Equation 4, the predicted HPBW is 48 millidegrees rather than the quoted 58 millidegrees. Since the quoted sidelobe levels of HUSIR reported in (Murray, Blackwell, Gaynor, & Kennedy, 2019) are considerably lower than that predicted by an Airy disk model as well, it can be inferred that HUSIR employs some form of illumination tapering. Illumination tapering is a

technique commonly used for reducing sidelobe levels at the expense of widening the beamwidth and decreasing the peak gain (Skolnik, 1990). Instead of adopting a tapered beam model and guessing the parameters of the tapering employed by HUSIR, the Airy disk beam model is retained and an effective diameter for HUSIR which results in the quoted 58 millidegree beamwidth is defined. This is justified since what is most important for these calculations is the angular location of the 3 dB point and not how the radiation pattern changes as a function of angular offset within the beam. A similar "effective diameter" technique has also been used with success by scientists at the Atacama Large Millimeter Array (ALMA) for modeling the beam patterns of the ALMA dishes (Brogan & Hunter, 2014). The effective diameter of the Airy disk beam model estimated for HUSIR is 30.5 m.

Using this model for HUSIR, the monostatic case was calculated which uses HUSIR as the transmitter and receiver. Table 2 presents the results of this calculation compared to the monostatic algorithm for HUSIR as a percent difference from the "truth" value of monostatic algorithm. The results were calculated for between 400 km and 700 km altitude with 50 km sized bins for both the 75E and 20S pointings as described earlier. All calculations were performed using 250,000 (500^2) equally spaced samples on the grid in each plane. The physical extent of the grid in space is set such that the slice of the beam pattern at the range of interest extends out to the first beam null. Since the grid extent is chosen dynamically as a function of range, the spatial point density may decrease but the angular point density remains constant. This has the effect of the error of this method being independent of the altitude of interest.

Table 2. Percent difference between the monostatic and bistatic lateral surface area calculations for two common pointings employed by HUSIR, 75E and 20S, between 400 km and 700 km with 50 km sized bins. Calculations performed with 250,000 points in the plane.

Start Altitude (km)	Stop Altitude (km)	% Difference for 75E	% Difference for 20S
400	450	0.449874	0.449876
450	500	0.449872	0.449876
500	550	0.449874	0.449876
550	600	0.449875	0.449876
600	650	0.449874	0.449877
650	700	0.449874	0.449877

As noted earlier, the calculation of the lateral surface area of the generalized bistatic beam overlap is performed in range space. Once the area has been computed, it is corrected by a factor of the cosine of the local angle with respect to the vertical. This method was chosen rather than to compute directly in altitude to remain consistent with the monostatic algorithm, which has the added benefit of making the error of this bistatic algorithm independent of the pointing for which the lateral surface area is calculated. In particular, all values in the error are the same to eight significant figures for each case presented in Table 2.

The major driver of the error of the lateral surface area calculation of the generalized bistatic beam model is the number of samples used in the plane for each perimeter calculation. Figure 12 shows the percent difference in the calculated areas as a function of the number of samples squared used in the plane. As the number of samples used in the plane increases, the error decreases asymptotically to zero. These results indicate that the bistatic algorithm converges to the monostatic algorithm in the monostatic case.

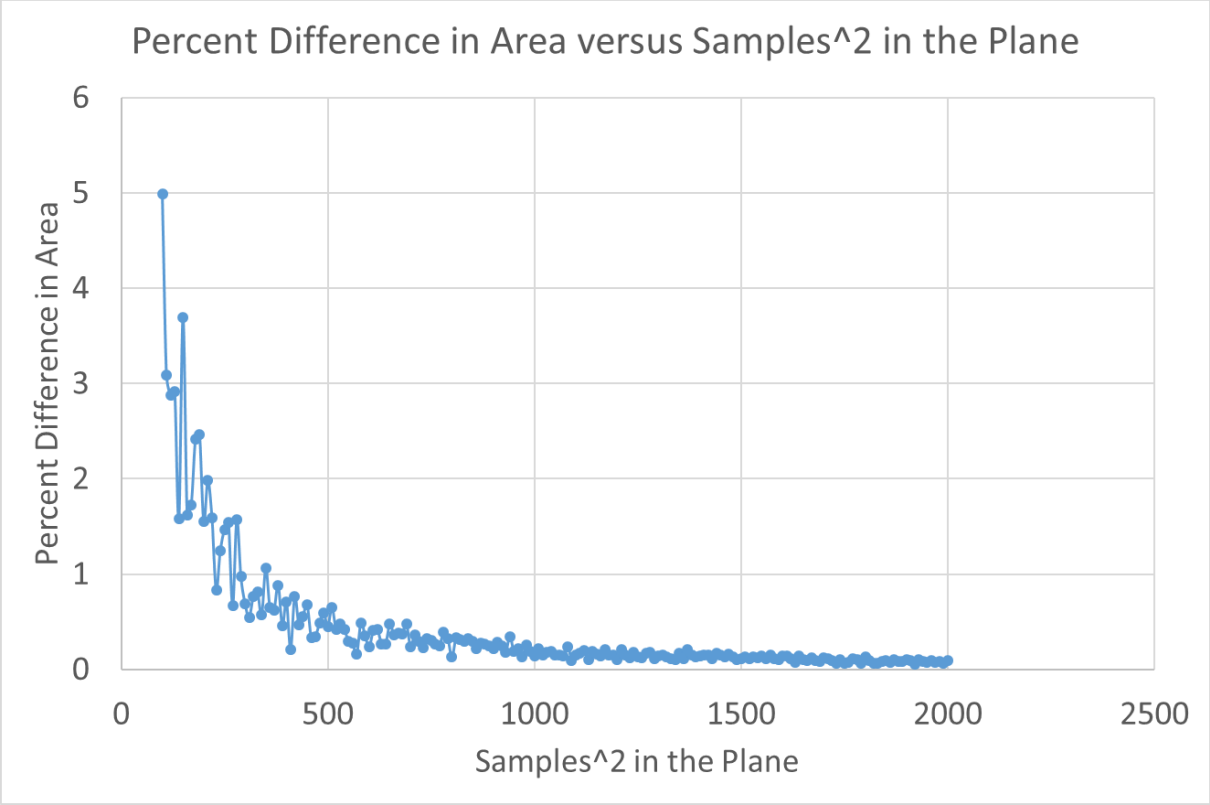

Figure 12. Percent difference between the monostatic and bistatic algorithms in the monostatic case as a function of the number of samples used in the plane.

Case Study: DSS-14/DSS-25

Prior to 2018, the transmitter and receiver employed by Goldstone, Deep Space Station (DSS)-14 and DSS-15, respectively, were sufficiently close to one another geographically to be considered quasi-monostatic. In 2018, DSS-15 was decommissioned and JPL began performing orbital debris radar observations using DSS-25 as a replacement receiver (Murray, 2019). As an application of this new method of lateral surface calculation, the lateral surface area of the main beam overlap of the Goldstone radar in the current configuration employed by JPL is calculated.

The current bistatic configuration of Goldstone uses DSS-14, a 70 m diameter dish, as the transmitter with a center frequency of 8.65 GHz. DSS-25, a 34 m diameter dish, is used as the receiver. The locations of both dishes are shown in Table 3 (Folkner, 2018). For orbital debris observations DSS-14 is pointed at an elevation of 75° and azimuth of 90°, similar to the 75E

pointing described for HUSIR (Miller, Murray, & Kennedy, 2021b). DSS-25 is pointed such the boresights of the antennas intersect at a slant range of 800 km from DSS-14.

Table 3. Geodetic Coordinates for Deep Space Network Stations with respect to the WGS 84 Ellipsoid.

Antenna	Latitude			Longitude			Height
Name	Deg	Min	Sec	Deg	Min	Sec	Meters
DSS-14	35	25	33.24312	243	6	37.66244	1001.390
DSS-25	35	20	15.40306	243	7	28.69246	956.634

The baseline between DSS-14 and DSS-15, the decommissioned receiver, was approximately 500 m. This enabled the transmitter and receiver pair cover the entire altitude extent of LEO with a single pointing. The current baseline between DSS-14 and DSS-25 is approximately 1.5 km, which severely reduces the instantaneous altitude coverage of an individual pointing. Figure 13 shows the normalized peak gain product of the DSS-14/DSS-25 pair as a function of altitude. In this figure, the approximate null-to-null beam overlap between the two antennas occurs between 700 km and 850 km altitude.

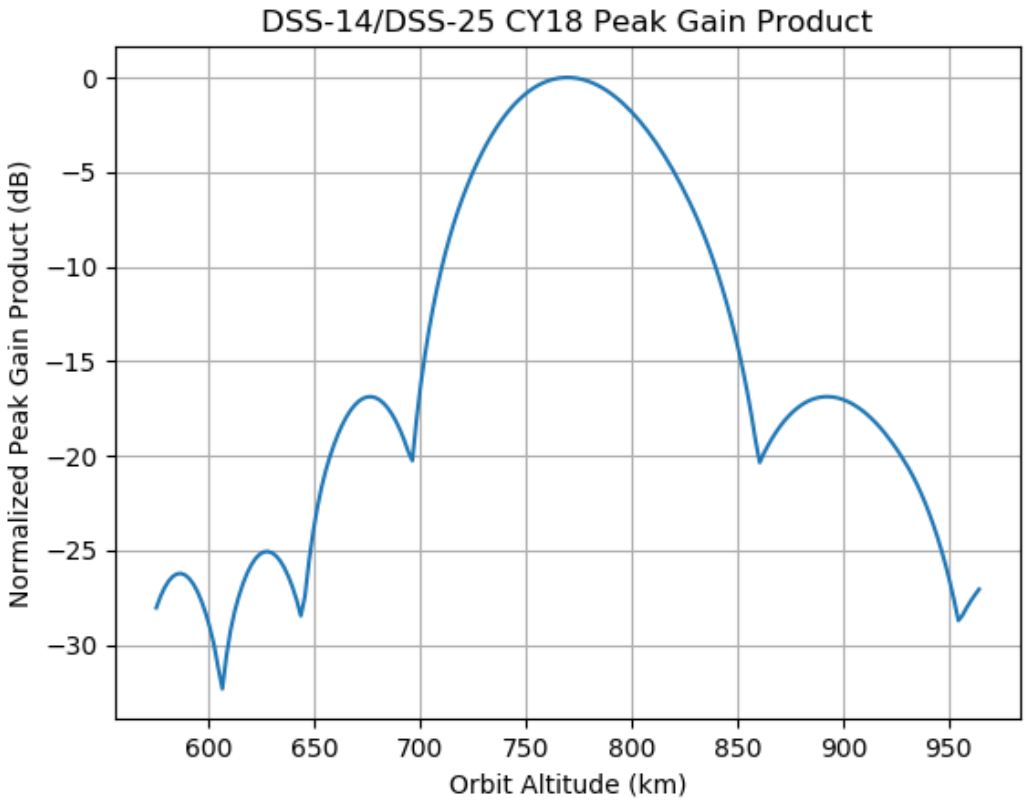

Figure 13. Normalized peak gain product of the DSS-14/DSS-25 antenna pair as a function of altitude.

When the baseline is short compared to the observation ranges, the opening angle of the frustum could be taken as the 6 dB point of the product of the transmitter and receiver's normalized radiation patterns as is done in (Kennedy, Murray, & Miller, 2020). For the bistatic lateral surface area calculation, the actual pointings and locations of the transmitter and receiver are used and the beams are modeled as Airy disks. The predicted beamwidth using the Airy disk model matches the quoted beamwidth in (Kennedy, Murray, & Miller, 2020).

Figure 14 shows an example frame-by-frame progression of the perimeter estimation from 750 km to 800 km altitude with eight cylinders: nine planes in total. Each frame plots the peak gain product as an interpolated image, with the grid of points at which the gain was calculated overlaid. Points outside the 6 dB surface are represented by a blue "+" symbol while those inside

are represented by a red "+" symbol. The points determined to be part of the convex hull are red stars and are connected by red lines which represent the estimated perimeter. Note the size of the red area increases moving toward the beam intersection altitude and decreases moving away from the beam intersection altitude.

For this comparison, the lateral surface area of the 6 dB surface between 700 km and 850 km altitude is calculated in 50 km wide bins. Each 50 km wide bin is sub-divided into 25 cylinders. Figure 15 shows the lateral surface area of the approximating cylinders overlaid on top of the normalized peak gain product shown in Figure 13, but as a function of slant range from DSS-14 rather than altitude. Note that the area goes to zero when the gain product goes below 6 dB. Another interesting feature is the peak lateral surface area does not occur at the same range as the peak gain product, but rather at a slightly higher range.

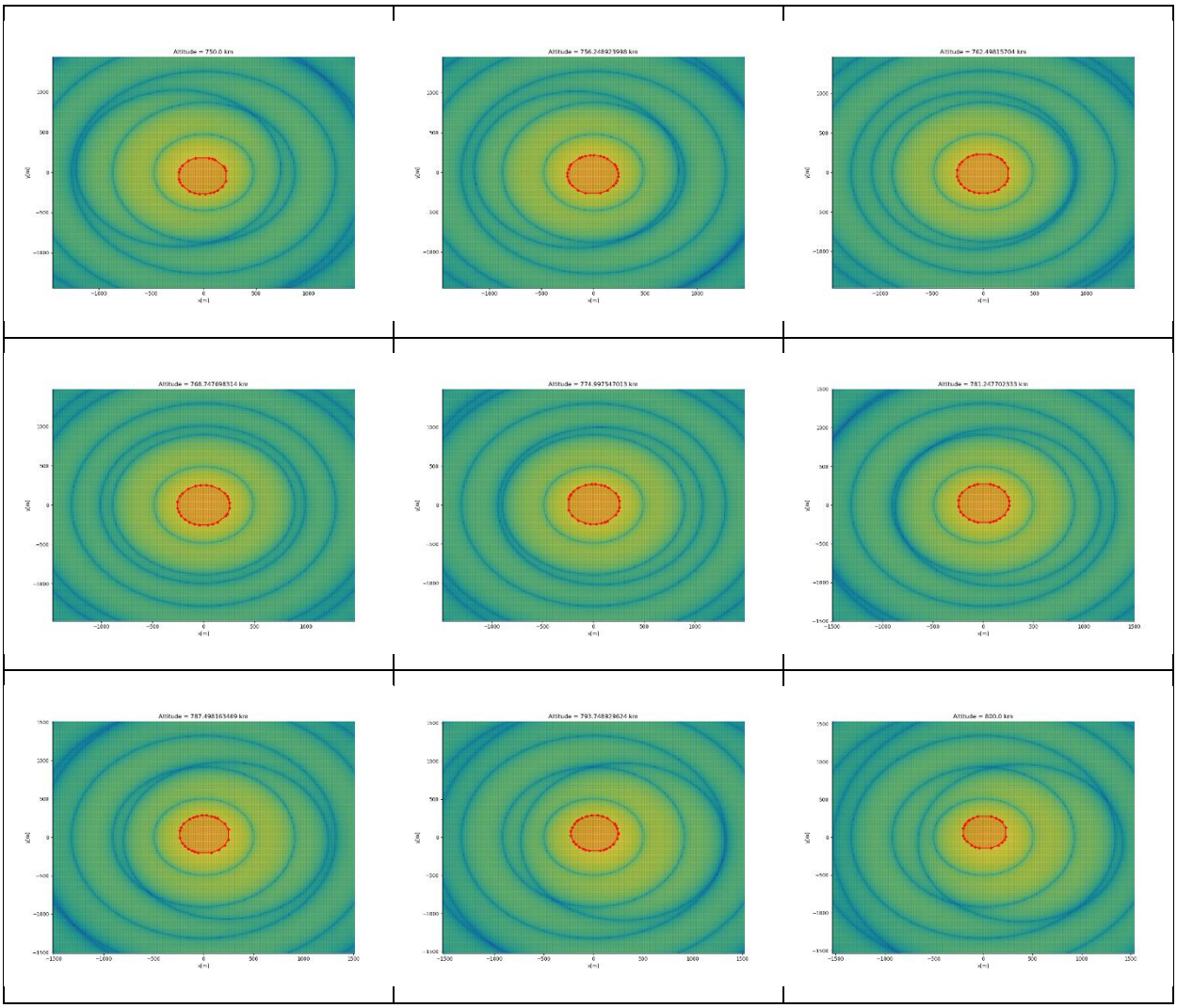

Figure 14. Example frame-by-frame progression of the perimeter estimation from 750 km to 800 km altitude with 8 cylinders, 9 planes in total.

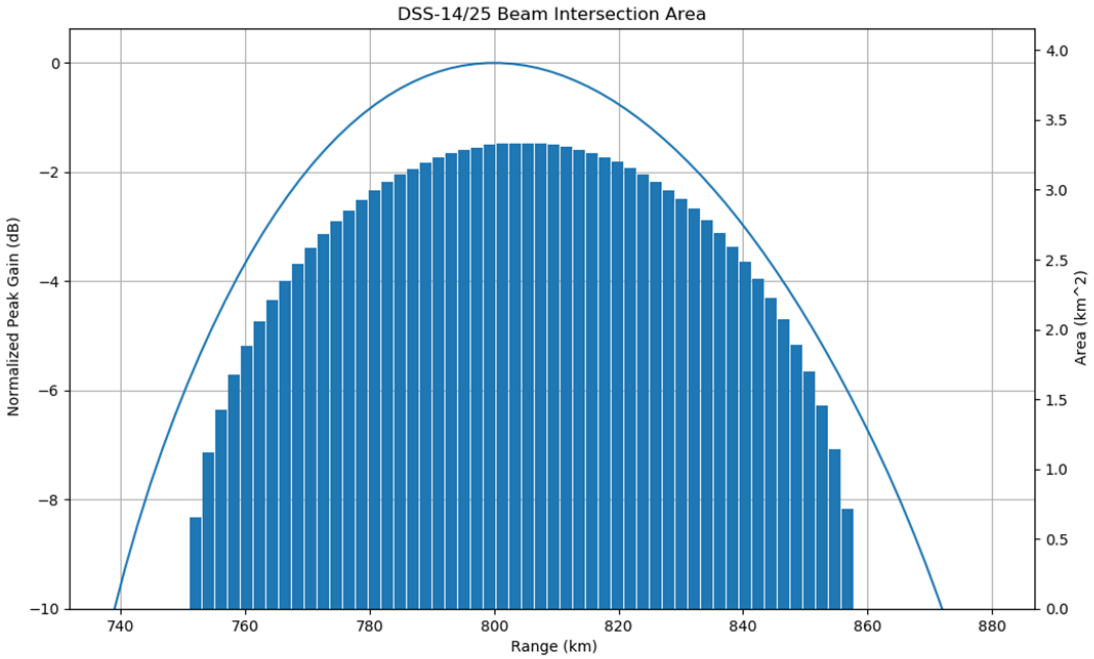

Figure 15. Lateral surface areas of the 2 km tall approximating cylinders as a function of slant range from DSS-14 overlaid on top of the peak gain as a function altitude.

Table 4 compares the results of the monostatic algorithm to those obtained with the generalized bistatic method. In the 750 km to 800 km altitude bin the two calculated areas are within 5% of each other. This is not surprising, as the beam intersection altitude is near the center of this altitude bin. The bistatic area of the adjacent altitude bins is lower than the monostatic area because the effective beam diameter is smaller the further one moves from the beam intersection point. In particular, the 6 dB surface only extends into portions of the 700 km to 750 km and 800 km to 850 km bins. These results show consistency with the monostatic approach in the altitude regimes where the beam overlap is considerable. The developed method represents a geometrically accurate representation of the lateral surface area of the bistatic beam overlap, defined by the 6 dB surface of the gain product.

Table 4. Comparison of Lateral Surface Area Calculations; Monostatic Method versus Generalized Bistatic Method.

Start Altitude (km)	Stop Altitude (km)	Monostatic Area (km^2)	Bistatic Area (km^2)
700	750	76.6	30.4
750	800	81.8	77.9
800	850	87.0	24.8

Total Error versus Baseline and Target Altitude

The error in total lateral surface area depends on many factors, including the baseline between the transmit and receive antennas and the target altitude for observation, as well as the direction in which the two antennas are pointed and the beamwidths of each antenna. A general guide was developed for total error versus baseline and target altitude, assuming Goldstone-type antennas pointed in a 75E-type observation configuration.

For simplification, the transmitter is placed at the equator pointed at 75° elevation eastward. The receiver is placed at several different baselines from 0 km (monostatic) out to 5 km eastward along the equator. At each baseline, target altitudes from 400 km to 1000 km in 100 km steps are chosen. For each baseline and target altitude pair, the receiver azimuth and elevation are set such that the receiver boresight intersects the transmitter boresight at the target altitude. Area as a function of altitude is then calculated from 300 km to 2000 km altitude (the entirety of LEO) in 50 km bins using both the monostatic method and the bistatic method. The areas of all bins are then integrated, and the percent error is calculated as the difference between the integrated monostatic calculated area and the integrated bistatic area divided by the integrated bistatic area. Figure 16 shows these results for percent error in integrated error as a function of baseline for 75E-type

pointings of Goldstone-type antennas for target altitudes from 400 km to 1000 km. As expected for higher target altitudes, the error increases more slowly than for lower target altitudes, where the intersection volume is smaller and bistatic angle is larger at the intersection point.

This chart can be used to determine, for a specific setup, at what baseline and target altitude would it become necessary to use the bistatic area calculation based on the specific error tolerance of the user application.

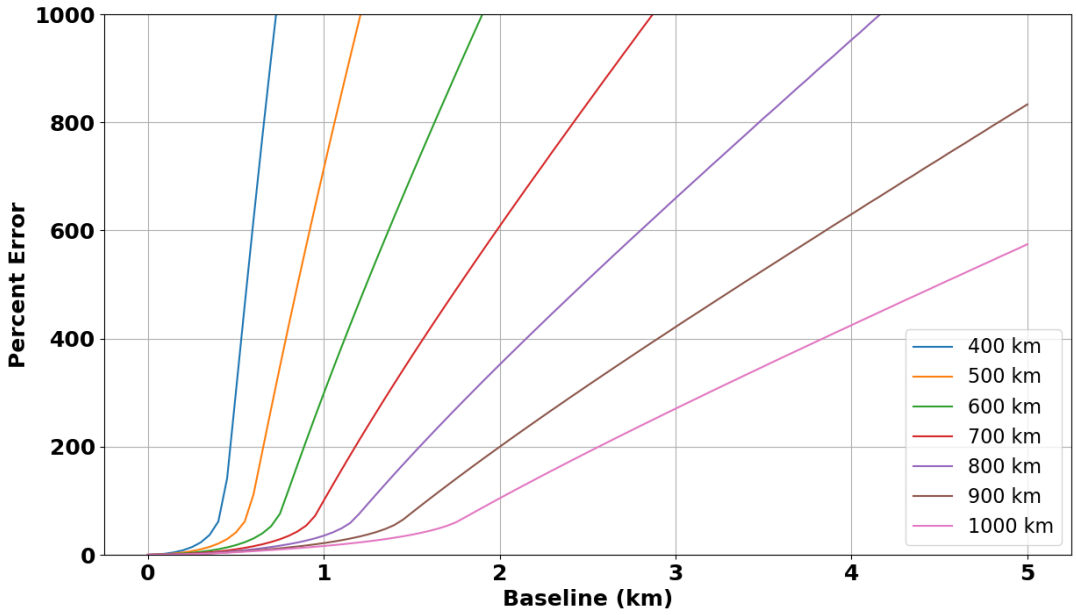

Figure 16. Percent error versus baseline for 75E type pointings of Goldstone antennas for target altitudes from 400 km to 1000 km.

Chapter Summary

Orbital debris engineering models are a critical tool in assessing the risk posed to spacecraft by orbital debris impacts. There exists a gap in the size coverage of existing data sources from 1 mm to 3 mm that results in large variations between competing orbital debris models in this size regime. Debris of this size also represent the highest mission-ending risk to spacecraft in LEO, making it of interest to investigate potential new orbital debris data sources.

Bistatic radar observations have been shown to increase the sensitivity of conventional terrestrial orbital debris radar measurements. There are many radars and radio telescopes that could be combined to create sensitive bistatic radars that could potentially bridge the 1 mm to 3 mm size gap. To evaluate the capabilities of a candidate sensor it is necessary to calculate its sensitivity and expected count rate, the latter of which requires calculating the lateral surface area of the sensor. An existing algorithm for calculating this area for a monostatic radar was presented.

A method for calculating the lateral surface area of a generalized bistatic radar was developed. The new method maps the radar beam overlap in 3D space by calculating the gain product of the transmitter and receiver at discrete points in space. By choosing points to lie on planes perpendicular to boresight one of the antennas, the lateral surface area was approximated using stacked polygonal cylinders. The perimeters of the bases of these cylinders were found using a convex hull algorithm on points in each plane. These perimeters were used to calculate the total lateral surface area.

The newly developed method was compared to the monostatic algorithm in the monostatic case. Two common observation configurations employed by HUSIR, 75E and 20S, were analyzed. Calculations showed that the results of the bistatic lateral surface area converged to the monostatic algorithm as the number of points in space increased. Furthermore, it was shown that the accuracy of bistatic method is independent of the pointing analyzed. It is also independent of the altitude for which the lateral surface area is calculated. This is due to the way in which off-vertical area corrections were handled in both the monostatic and newly developed bistatic methods, as well as choosing a constant angular point density for points in the plane.

The new method was also applied to the DSS-14/DSS-25 bistatic observation configuration currently employed by Goldstone. The lateral surface area of the 6 dB surface between 700 km

and 850 km altitude in 50 km wide bins was calculated. Each 50 km wide bin was sub-divided into 25 cylinders. In the center altitude bin, areas were within 5% of the monostatic lateral surface area calculation. In adjacent bins the area is significantly lower. This is due to the effective narrowing of the beam diameter as one moves away from the beam intersection point.

A general guide was developed for total error versus baseline and target altitude, assuming Goldstone-type antennas pointed in a 75E-type observation configuration. The general guide can be used to determine (for a specific setup) at what baseline and target altitude would it become necessary to use the bistatic area calculation based on the specific error tolerance of the user application.

Results indicate that this newly developed bistatic method provides a geometrically accurate representation of the lateral surface area of a bistatic radar system, as defined by the 6 dB gain product surface. The flexibility of this method will make it useful for planning orbital debris radar observations, particularly for novel bistatic radar observation configurations.

CHAPTER THREE:

SENSITIVITY-LIMITED COUNT RATE ESTIMATION

Two of the key performance metrics evaluated to determine the utility of a radar for orbital debris measurements are the minimum detectable size and the total count rate expected for an observation. The size of an object is not a directly measurable parameter using a radar. Radar measures an object's RCS. In general, the RCS of an object depends on not just its size, but also its reflectivity and shape. The NASA SEM is used to simplify the relationship between the two parameters. The NASA SEM creates a one-to-one mapping between debris size and RCS for radar measurements of orbital debris. The minimum detectable size is mostly dependent on the sensitivity of the radar, making such calculations straight forward if one knows the relevant transmitter and receiver parameters.

It is important to estimate the expected count rate because even if a radar is extremely sensitive, it must be able to collect a statistically significant sample within a reasonable time. It turns out that total count rate is a more complex calculation than the minimum detectable size. It requires not only the sensitivity of the radar, but an estimate of the altitude dependent flux of debris on orbit as a function of size, the geometry of the beam intersection, and a model of the time-dependent RCS variation behavior of the target and its effect on the probability of detection. Expected debris flux is estimated from ORDEM. ORDEM's "Telescope Mode" can be used to estimate flux of debris as a function of both altitude and size. All that is required is the radar's location and pointing direction.

Knowing the expected flux of debris through the radar beam, the fraction of that debris the radar would be able to detect is calculated from the radar sensitivity. This results in a "detectable debris" flux. As mentioned previously, flux is related to count rate though the calculation of the

lateral surface area. This is done for each altitude bin and then integrated over altitude to estimate a total count rate of debris expected for a radar debris observation.

In this Chapter, a formula for minimum detectable RCS is derived and the NASA SEM that is used for RCS-to-size conversions is described. Next, NASA's ORDEM and how it can be used to calculate flux estimates for radar observations, is presented. Then, a procedure for calculating a sensitivity-limited total count rate is derived. Finally, the developed methods are validated against actual debris data collected by the HUSIR radar.

Minimum Detectable Radar Cross-Section

The radar equation generalized for bistatic radar is given by (Skolnik, 1990) as

$$\mathrm{P}_r = \mathrm{P}_t \frac{\mathrm{G_t\, G_r\, \sigma\, \lambda^2}}{(4\pi)^3\, \mathrm{R_t^2\, R_r^2}}, \qquad (6)$$

where P is power, G is gain, R is the slant range, λ is the wavelength, and σ is the bistatic RCS. The t and r subscripts refer the transmitter and receiver respectively. Assuming that the primary noise contribution comes from thermal noise in the receiver, one can divide the expression by receiver noise power to obtain an expression for the Signal-to-Noise Ratio (SNR). Including system losses, the expression can then be rearranged to isolate the minimum detectable RCS which gives

$$\sigma_{min} = SNR_{min} \frac{(4\pi)^3\ \mathrm{R_t^2\, R_r^2\, k_B\, T_{sys}\, \Delta f_r\, L}}{\mathrm{P_t\, G_t\, G_r\, \lambda^2}}, \qquad (7)$$

where T_{sys} is the receiver system temperature, k_B is Boltzmann's constant, $\Delta \mathrm{f_r}$ is the receiver bandwidth, and L is the total system loss. The total system loss is a combination of losses including transmit losses, receive losses, atmospheric losses, scanning losses, range-gate straddling losses, Doppler straddling losses, collapsing losses, signal processing losses, and other miscellaneous losses. Here, an average loss of 9 dB is included to account for all of these factors.

Additionally, a minimum SNR of 10 dB is chosen. It should be noted that this applies to a single pulse detection at the peak gain of both the transmitter and receiver.

Minimum Detectable Size

The size estimation is based on the NASA SEM. This model creates a one-to-one mapping of RCS to characteristic length/size, where characteristic length is defined as the average of the three longest orthogonal lengths of an object. An illustration of the geometry involved in the calculation of characteristic length is shown in Figure 17, where x is defined as the longest projection dimension, y as the longest projection dimension perpendicular to x, and z as the longest projection dimension orthogonal to both x and y.

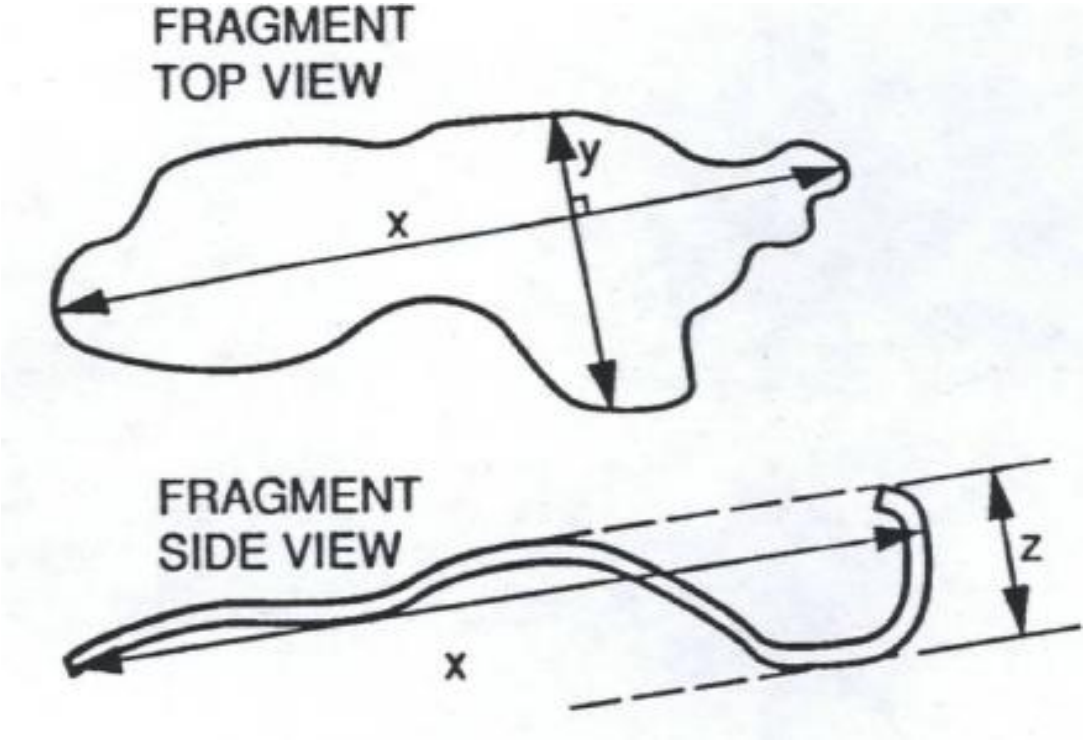

Figure 17. Illustration of body and projected measurement on complex shape used in determining characteristic length. (McKnight, Johnson, Fudge, & Maclay, 1995)

The SEM originated from RCS measurements of two U.S. Department of Defense hypervelocity impact tests of simulated satellites conducted in the early 1990's that utilized

representative debris objects (Bohannon, Caampued, & Young, 1994) (Dalquist & Bohannon, 1991). RCS measurements were performed on 39 representative debris objects over four commonly used radar frequency bands, S-band, C-band, X-band, and Ku-band with eight frequency samples taken in the lowest frequency band and sixteen frequency samples taken in the remaining three frequency bands. These radar frequency bands correspond to the frequency bands used by orbital debris radars at the time. The measurements were taken at several orientations to understand the RCS distributions for each piece of debris to best represent the RCS distribution presented to a radar by a tumbling piece of debris passing through the radar in a beam-park observation (Barton, et al., 1998) (Everett, Caampued, & Chu, 1991) (Everett, Dalquist, & Caampued, 1991). Radar data taken at different frequencies can be compared by scaling the characteristic size and RCS by the measurement wavelength. Figure 18 shows the wavelength-scaled results of RCS-to-size measurements on 39 representative debris objects taken at various orientations resulting in 2072 data points. The blue curve represents the RCS-to-size relationship of a perfectly conduction sphere, whereas the black curve represents a weighted polynomial fit to the measurements comprising the NASA SEM.

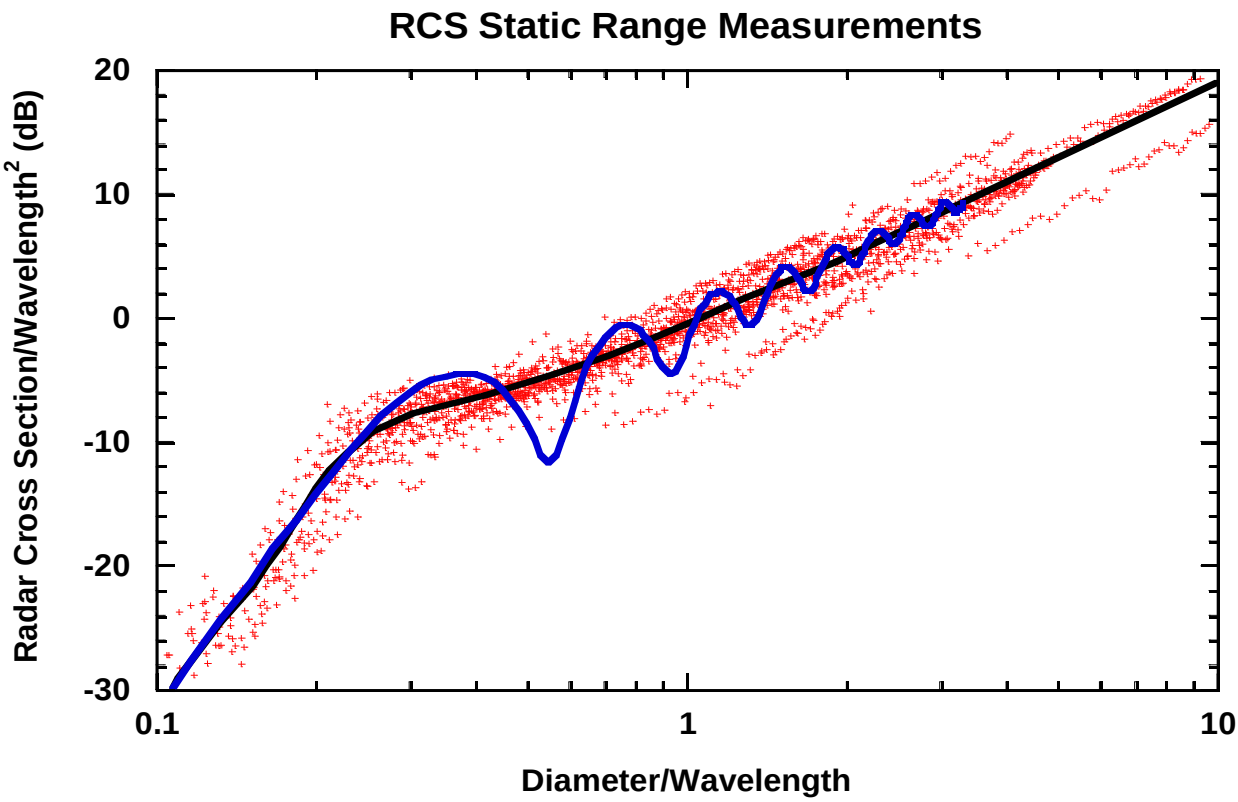

Figure 18. Results of RCS-to-size measurements on 39 representative debris objects. The oscillating line is the RCS for a spherical conductor while the smooth line is the polynomial fit to the data. (Murray & Kennedy, 2021)

The NASA SEM is a piecewise function given by

$$x = \sqrt{\frac{4z}{\pi}}, \text{ for z>2. 835, Optical Regime}$$

$$x = \sqrt[6]{\frac{4z}{9\pi^5}}, \text{ for z< 0.00122, Rayleigh Regime}$$

$$x = g(z), \text{ in between, Mie Regime}$$

where $z = RCS/\lambda^2$, $x = diameter/\lambda$, and λ is wavelength. The smooth function $g(z)$ is expressed by 23 points in Table 5. An example of the NASA SEM for UHF, S-band, and X-band is shown in Figure 19.

Table 5. The NASA SEM curve x=g(z) in the Mie resonance region. (Murray, Blackwell, Gaynor, & Kennedy, 2019)

$z=RCS/\lambda^2$	x=diameter/λ
0.10997	0.001220
0.11685	0.001735
0.12444	0.002468
0.13302	0.003511
0.14256	0.004993
0.15256	0.007102
0.16220	0.01010
0.17138	0.01437
0.18039	0.02044
0.18982	0.02907
0.20014	0.04135
0.21237	0.05881
0.22902	0.08365
0.25574	0.1190
0.30537	0.1692
0.42028	0.2407
0.56287	0.3424
0.71108	0.4870
0.86714	0.6927
1.0529	0.9852
1.2790	1.401
1.5661	1.993
1.8975	2.835

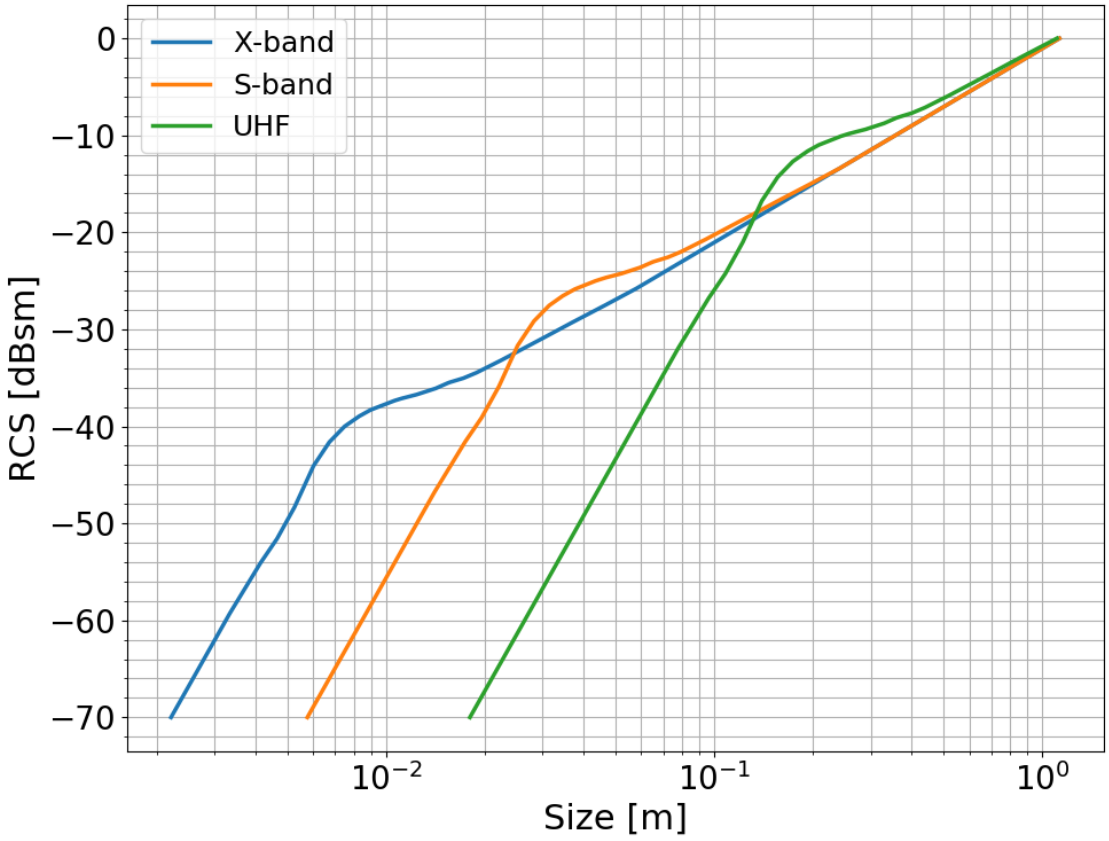

Figure 19. NASA SEM for UHF, S-band, and X-band: RCS-to-Size conversion.

Observational Surface Area

ORDEM flux output for LEO can be binned in either 50 km or 5 km wide bins. Here the 5 km bin size is used to better capture the bistatic effects on sensitivity and area as a function of altitude. For the area calculations, 25 approximating cylinders per altitude bin are used with 62,500 (250^2) points sampled in each plane. The mathematical details of the calculation were presented in Chapter Two.

Debris Detection Rate

NASA publishes a software called the Orbital Debris Engineering Model (ORDEM), currently in its 3rd version (Vavrin, et al., 2019), with the most recent release being ORDEM 3.1.

ORDEM can be used in "Telescope Mode" to retrieve the modeled debris flux as a function of altitude and debris size for a radar using the radar's geographic coordinates and its pointing direction. A representative ORDEM output is shown in Figure 20. The flux calculated by ORDEM is the flux through the lateral surface area of a conical frustum whose opening angle is the 2-way 6 dB beam width of the radar/telescope.

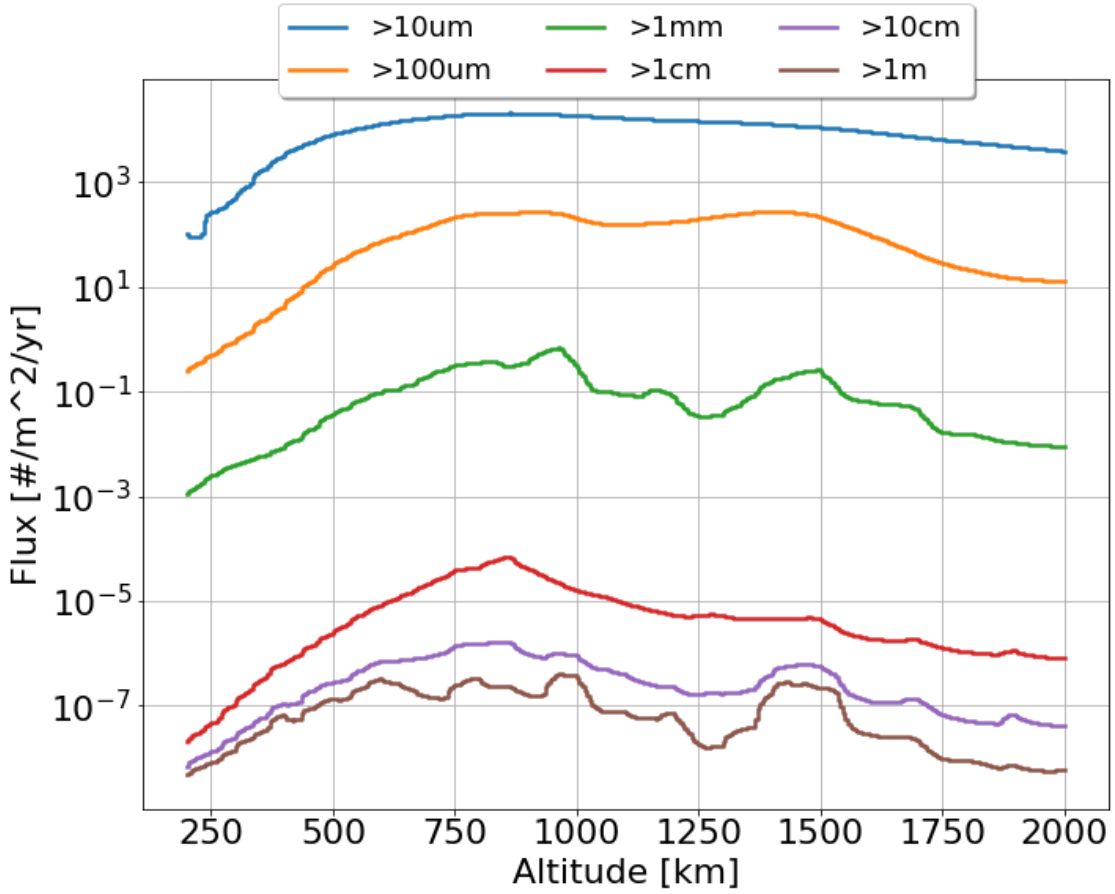

Figure 20. Cumulative Flux of Debris to decadal limiting sizes as computed by ORDEM for a sensor located at 18.444° latitude pointed at 90° elevation in 2018.

ORDEM output in telescope/radar mode is a cumulative flux as a function of debris size and altitude, where flux is number of debris per unit area per unit time. Cumulative flux represents the flux of debris of a given size and larger and is defined as

$$F(h,l) = \int_{l}^{\infty} f(h,l')dl' \ , \quad (8)$$

where F is the cumulative flux, f is the flux density, h is altitude, and l is debris size. ORDEM only calculates cumulative flux in decade steps from 10 μm to 1 m. For the proceeding calculations, the flux is first interpolated from the six provided fiducial points to 1000 logarithmically spaced points using the Piecewise Cubic Hermite Interpolating Polynomial (PCHIP) algorithm (Fritsch & Butland, 1984). This algorithm was chosen because it preserves monotonicity which is important when interpolating cumulative curves. After this, to predict a total count rate the lateral surface area as a function of altitude, $A(h)$, is computed. Additionally, sensitivity of the radar must be taken into account by computing a probability of detection, P_D. Since it is a function of debris size, one integrates over the product of the probability of detection and flux density to estimate sensitivity limited cumulative flux, or "detectable flux". Flux density is recovered from cumulative flux through differentiation.

$$f(h,l) = -\frac{dF}{dl} \quad (9)$$

Single pulse probability of detection is calculated using non-central chi-squared distribution with 4 degrees of freedom depending on SNR_T, the SNR threshold used to declare a detection, and the actual SNR. SNR can be estimated using the bistatic radar equation

$$SNR = \frac{P_t G_t G_r \lambda^2 \sigma F_t^2 F_r^2}{(4\pi)^3 k_B T_s \Delta f R_t^2 R_r^2 L} \ , \quad (10)$$

where P_t is the peak transmit power, G is the peak gain, λ is the wavelength, F is the pattern propagation factor, k_B is Boltzmann's constant, T_s is the system temperature, Δf is the receiver bandwidth, R is range to target, L is a general loss term, σ is the RCS, and the t and r subscripts indicate the transmitter and receiver, respectively. RCS is related to the debris size using the NASA

SEM which is a function of RCS and radar wavelength. Since the SEM gives a one-to-one mapping between RCS and size, one can invert the SEM to estimate the RCS of debris of a certain size.

$$l = SEM(\sigma, \lambda) => \sigma = SEM^{-1}(l, \lambda) \quad (11)$$

Combining everything, for each ORDEM debris size, its RCS is estimated. From the RCS and transmitter/receiver characteristics, the SNR that would be measured by the radar is calculated. This SNR along with the SNR threshold used for detection declaration is used to compute the probability of detection for the debris size. The sensitivity limited cumulative flux is then calculated as

$$F'(h, l) = \int_{l}^{l_0} f(h, l') P_D(l') dl' + F_0(h) \quad (12)$$

Since one cannot numerically integrate to infinity, the integral for F is split at l_0, the largest size for which ORDEM provides a cumulative flux, where $F_0(h) = \int_{l_0}^{\infty} f(h, l') P_D(l') dl' = \int_{l_0}^{\infty} f(h, l') dl'$ is the cumulative flux at the largest size for which ORDEM provides a cumulative flux and assumes probability of detection at this size to be 1. Figure 21 shows a representative cumulative flux versus size output from ORDEM in a single altitude bin, where the black dots represent the fiducial points calculated by ORDEM, the blue curve represents the PCHIP interpolated flux, the orange curve represents the sensitivity-limited cumulative flux, and the red star represents the estimated minimum detectable size.

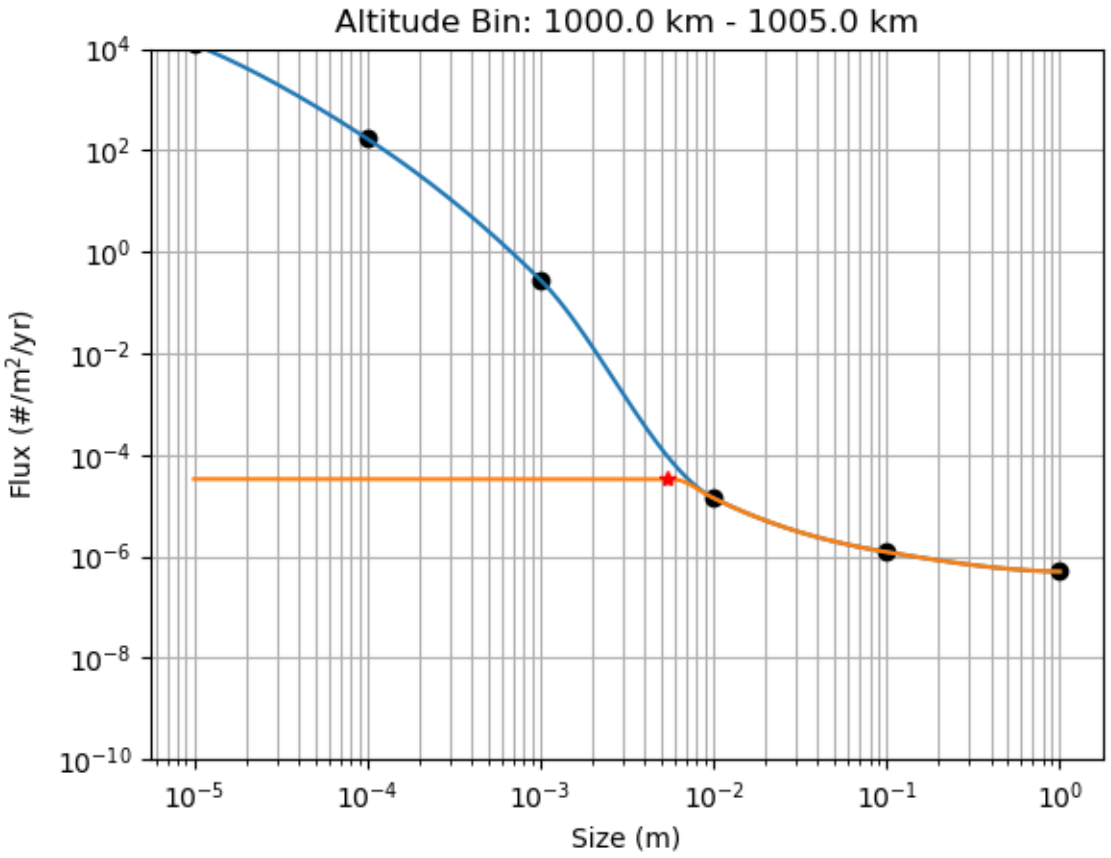

Figure 21. Representative cumulative flux versus size output from ORDEM in a single altitude bin, where the black dots represent the fiducial points, the blue curve represents the PCHIP interpolated flux, the orange curve represents the sensitivity-limited cumulative flux, and the red star represents the minimum detectable size.

Cumulative count rate is calculated by integrating the cumulative flux/area product over altitude.

$$\dot{N}(l) = \int_{h_0}^{h_1} A(h)F'(h,l)dh \quad (13)$$

Area is calculated as described in Chapter Two. Assuming that the product $f(h,l)P_D(l)$ approaches zero as l approaches zero, the total count rate, $\dot{N}_T$, is estimated by taking the limit of the cumulative count rate as l approaches zero.

$$\dot{N}_T = \lim_{l \to 0} \dot{N}(l) \quad (14)$$

HUSIR Predictions and Validation

Results published by NASA (Murray & Kennedy, 2020) for data taken in 2018 are used as a validation source. HUSIR consists of a 36.6 m dish with a monopulse feed horn used to detect the location of an object within the beam using amplitude comparison monopulse techniques. HUSIR transmits a pulsed continuous wave waveform with a center frequency of 10 GHz and a nominal peak power of 250 kW. The operating parameters for debris measurements for HUSIR are shown in Table 6.

Table 6. Radar Debris Mode Nominal Operating Parameters. Waveform Code is an internal designation used by MIT/LL. Range Gates refers to the number of overlapping range windows or "gates" in the Range-Doppler Image used by the real-time processor for detection. (Murray & Kennedy, 2020)

Operating Parameter	HUSIR
Peak Power (kW)	250
Transmitter Frequency (GHz)	10.0
Transmitter Wavelength (cm)	3.0
Antenna Diameter (m)	36.6
Antenna Half-power beam width (deg)	0.058
Antenna Gain (dB)	67.23
System Temperature (K)	186
Total System Losses (dB)	3.9
Waveform Code	4
Range Gates	16
Intermediate Frequency Bandwidth (kHz)	1250
Independent Range/Doppler Samples	15158
FFT Size	16384
Number of non-coherently integrated pulses used for detection	16
Pulse Width (msec)	1.6384
Receive Window (msec)	12.1264
Pulse repetition frequency (Hz)	60
Nominal Sensitivity (dB)	59.2
Average Power (kW)	24.6
Doppler Extent (km/s)	±7.5

For debris observation, HUSIR points in a fixed direction and allows the debris environment to pass through the stationary radar beam. This is done to present a fixed volume,

simplifying the calculation of debris flux. HUSIR collects most of its data pointing at 75° elevation, due East, referred to as 75E. The 75E geometry allows the radar to measure Doppler shifts that give meaningful orbital information for orbital inclinations between approximately 40° inclination and 140° inclination.

Data is collected by MIT/LL using a real-time processor, which records data in a circular buffer until a pre-determined SNR threshold is exceeded. Once the SNR threshold is crossed, the buffer is saved and continues to be saved as long as the SNR threshold is exceeded. The detector non-coherently integrates 16 pulses to improve sensitivity. The data collected by MIT/LL is then sent to NASA for calibration and processing.

To validate the methods that have been developed, predictions for the performance of HUSIR in CY2018 are compared to the results contained within (Murray & Kennedy, 2020). Total observation time, number of detections, and corresponding detection rate for the data presented in the report are shown in Table 7. The number of detections represents the total number of events for which there were three or more pulses with an integrated SNR greater than 5.65 dB, where at least one is in the two-way, 6 dB-beamwidth.

Table 7. Summary of HUSIR data taken in 2018.

Observation Time in 2018	313.2 hours
Total Number of Detections in 2018	4964 detections
Measured Detection Rate in 2018	15.85 per hour

Predictions based on the previously described methods are shown in Table 8. The estimates are within approximately 2% of the reported detection rate for that year, indicating the total detection rate calculation is performing well. Additionally, the calculated minimum detectable size of 5.43 mm matches well with the reported 5.5 mm minimum size.

Table 8. Predicted HUSIR Performance for 2018 Observations.

Minimum RCS @ 1000 km	-47.34 dBsm
Minimum Size @ 1000 km	5.43 mm
Intersection Area	6303.95 km^2
Total Count Rate	16.07 per hour

Figure 22 shows altitude-integrated sensitivity-limited cumulative count rate estimate for HUSIR 75E CY2018 observations. A sensitivity roll-off can be seen near about 5.5 mm. Figure 23 shows the cumulative count rate as a function of SEM size as measured by HUSIR at 75E in CY2018. A similar shape in the distributions overall, including a similar sensitivity roll-off. One feature of interest is while ORDEM only predicts flux for objects as large as 1 m, HUSIR measured objects as large as about 10 m.

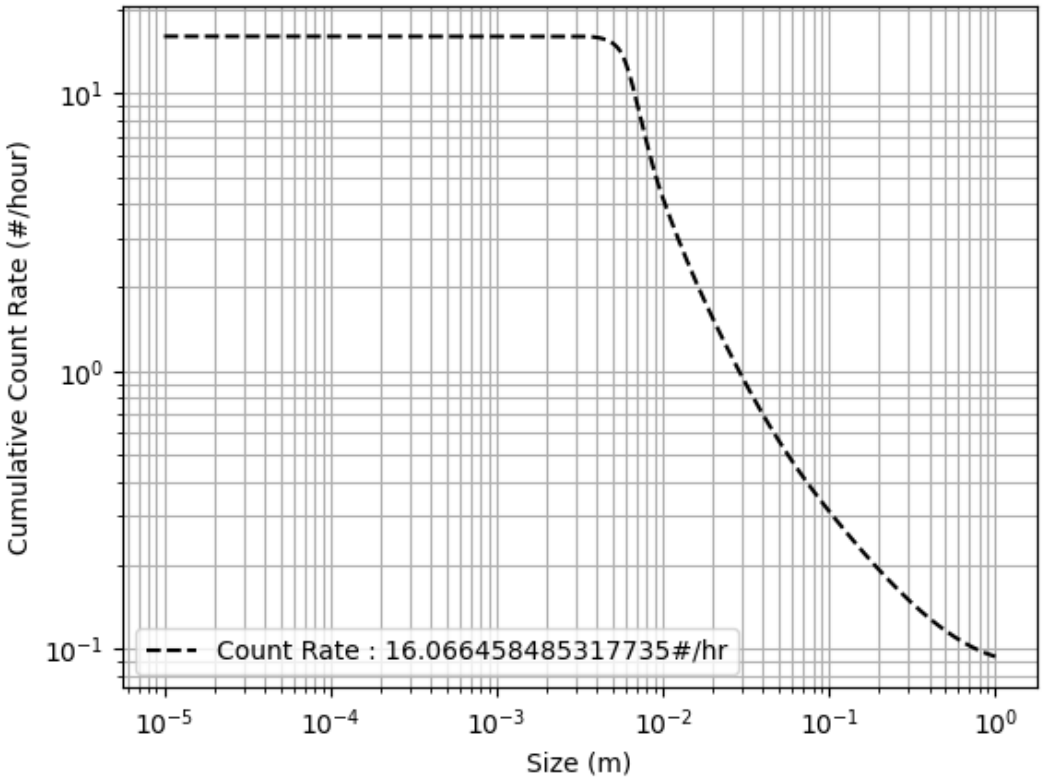

Figure 22. The altitude-integrated sensitivity-limited cumulative count rate estimate for HUSIR 75E CY2018 observations.

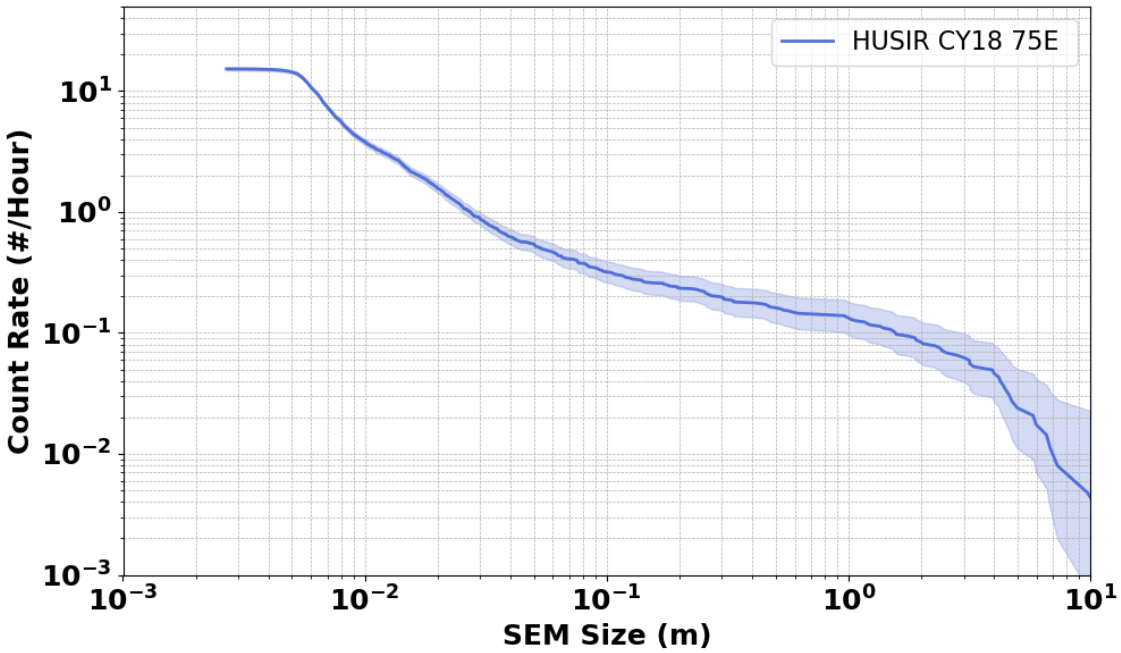

Figure 23. Cumulative count rate as measured by HUSIR at 75E in CY2018. The shaded regions represent the Poisson 2σ confidence intervals. (Murray & Kennedy, 2020)

Chapter Summary

To determine the efficacy of a radar for statistical measurements of the orbital debris environment in LEO, one must estimate the minimum size of debris able to be detected by the radar and the total count rate expected during an observation. Calculation of minimum detectable size shows whether a radar is sensitive enough to measure debris populations of interest. Total count rate is calculated to determine whether statistically significant information can be gathered in a reasonable amount of time. To calculate these parameters, one needs the sensitivity of the radar, an estimate of the altitude dependent flux of debris on orbit as a function of size, the geometry of the beam intersection, and a model of the time-dependent RCS variation behavior of the target and its effect on the probability of detection.

In this Chapter, methods of calculating minimum detectable size and total count rate were developed. A formula for minimum detectable RCS was derived and the NASA SEM (used for

RCS-to-size conversions) was described. NASA's ORDEM was introduced and used to calculate flux estimates. A method to relate the flux of debris on orbit to a cumulative count rate using the radar sensitivity, probability of detection, and radar lateral surface area was shown.

Data taken by HUSIR in CY2018 was used as a source of validation for the developed methods. The observation geometry, relevant radar parameters, and detection methodology employed by HUSIR for the observations were described. Results of the HUSIR observations were presented and compared to predictions. The estimated minimum detectable size matched well with the minimum size presented in the NASA report. The total count rate estimate was within 2% of the measured count rate. Results indicated the developed methods perform well.

CHAPTER FOUR:

ARECIBO PERFORMANCE ESTIMATES

The Arecibo Observatory had one of the largest and most sensitive radio instruments in the world which allowed the Arecibo Observatory to push the boundaries of knowledge in astronomy, atmospheric science, and planetary science. Unfortunately, much of these capabilities are no longer currently available due to the recent collapse of the Arecibo dish, now referred to as the Legacy Arecibo Telescope (LAT). There is, however, a proposal for a replacement instrument called the Next Generation Arecibo Telescope (NGAT). The NGAT promises improved radar performance over the already substantive legacy system. For orbital debris observations, the location of the Arecibo Observatory would allow the measurement of an under-sampled range of orbital inclinations at all sizes. Furthermore, the NGAT could bridge the gap between the sub-millimeter *in-situ* data and the greater than 3 mm terrestrial radar data and provide validation of orbital debris environment models in the size regime which poses the highest risk of penetration to most spacecraft.

In this Chapter, overview of the Arecibo Observatory is given and the systems of the LAT are described. Previous measurements of orbital debris and meteors using the LAT, as well as orbital debris experiments performed with other radio telescopes are also discussed. Next, the proposed NGAT system and its improvements of interest are described. The performance metrics of interest for orbital debris measurements and how they are calculated are then reviewed. These metrics for various configurations of the LAT and NGAT are then estimated and compared to predicted HUSIR performance. Finally, it is shown that with a few additional hardware upgrades to the proposed NGAT system, it would be possible to measure debris as small as 1 mm, potentially making it the most sensitive terrestrial radar for orbital debris measurements.

The Arecibo Observatory

The LAT was a 305 m diameter spherical dish built into a natural sinkhole near Arecibo, Puerto Rico. The dish was originally designed to be an Ultra High Frequency (UHF) ionospheric radar, which featured a 430 MHz line feed suspended by steel cables at the focal line. Upgrades were made over several years, one of which included a dome containing several receivers and Gregorian optics designed to correct the spherical aberration of the original optics. Since the dish was stationary, pointing was performed by moving the receivers to different focal points above the dish. This impacted both the slew rate and the zenith angle over which the dish could point. A summary of the dish location and structure are provided in Table 9.

The Arecibo Observatory is located at 18.3° N latitude which is significantly closer to the equator than both the HUSIR and Goldstone radars. As a rule of thumb, the inclination limit of a radar is roughly equal to the radar latitude. One can define the fraction of visible orbital inclinations as

$$\delta i = 1 - \frac{\phi}{90°}, \quad (15)$$

where ϕ is the sensor latitude. By this metric HUSIR, Goldstone, and Arecibo can observe approximately 53%, 61%, and 80% of all orbital inclinations. The location of the Arecibo Observatory increases its percentage of visible orbital inclinations by 27% compared to HUSIR.

Table 9. General Information of the LAT. (Salter, 2020)

Coordinates	
Latitude	18° 20’ 36.6” N
Longitude	66° 45’ 11.1” W
Azimuth Slew Rate	0.4°/s
Elevation Slew Rate	0.04°/s
Zenith Angle Range	0.0° – 19.69°
Reflector and Structure	
Type	Fixed reflector, movable feeds
Diameter of Reflector	1000 ft (304.8 m)
Area of Aperture	18 acres (73,000 m^2)
Shape of Surface	70° spherical cap
Radius of Curvature	870 ft (265 m)
Surface Accuracy	2.2 mm rms

Radars of the Legacy Arecibo Telescope

S-band Radar

The S-band Radar was a planetary radar primarily used for the measurement and imaging of solar system bodies. Both the transmitter and receiver were located on the rotary floor of the Gregorian dome. Diplexing was performed by rotating the transmitter out of the focus and the receiver into it. This process took a minimum of 4 seconds, which made it impossible to view objects in LEO. The radar could be operated in a bistatic mode to overcome this limitation.

An experiment such as this was performed in 1992 (Thompson, Goldstein, Campbell, Stansbery, & Potter, 1992) as a proof of concept for using terrestrial radar for orbital debris measurements. The receive antenna was a 30.5 m parabolic reflector located 10.7 km North-Northeast of the main antenna. The two dishes were pointed slightly off zenith such that their beam intersected at approximately 575 km and covered a range of 500-1000 km in altitude. The experiment was conducted over 3 observations for a total of 18.8 hours. During this time 90 objects from 5 mm to 20 cm were detected for a total rate of 4.79 per hour. The size was calculated assuming metallic spheres in the Rayleigh scattering regime, as this experiment predates the

NASA SEM for orbital debris. At the time of the experiment the transmit power was only 400 kW. The observatory had several upgrades after this experiment, including an increase in transmission power. The most recent capabilities of the S-band planetary radar, prior to collapse, are shown in Table 10.

Table 10. LAT S-band Radar Parameters.

Frequency	2038 MHz
Bandwidth	10 MHz
Polarization	Circular
Peak Gain	73.7 dB
Half-Power Beam Width	1.9 arcmin
System Temperature	20 K
Peak Power	1 MW
Average Power	1 MW
Max Duty Cycle	100%

UHF Radar

The UHF radar was primarily an incoherent scatter radar used to study the ionosphere. The radar has also been used for measurements of the moon, near-Earth asteroids, and meteors. The first reported use of the system for meteor observations was reported in 1995 (Zhou, Tepley, & Sulzer, 1995) where meteor ablation trails were observed in the 80-120 km altitude range. Since then, additional observations have been performed and analysis techniques have been developed by (Zhou & Kelley, 1997), (Janches, Mathews, Meisel, & Zhou, 2000), (Sulzer, 2004), (Wen, Doherty, & Mathews, 2004), (Wen, Doherty, & Mathews, 2005), (Wen, Doherty, Mathews, & Janches, 2005), and (Briczinski, Mathews, & Meisel, 2009) proving the UHF radar of the LAT to have been a crucial instrument to the study of radar meteors.

Power from the UHF transmitter could be routed to the line feed, the dome feed, or both simultaneously in a dual beam or "dual radar" configuration by way of a power splitter. The line feed had greater gain at zenith than the dome feed due to its greater aperture filling factor. As the

line feed moved away from zenith, the gain decreased and the system temperature increased due to illumination spill-over. Although this happened to some extent with the dome feed, the effect was diminished because the dome feed illuminated a smaller portion of the dish.

Table 11. LAT UHF Radar Parameters.

Frequency	2038 MHz
Bandwidth	10 MHz
Polarization	Circular
Peak Gain	73.7 dB
Half-Power Beam Width	1.9 arcmin
System Temperature	20 K
Peak Power	1 MW
Average Power	1 MW
Max Duty Cycle	100%
Max Pulse Repetition Frequency	1 kHz
Maximum Pulse Length	2.1 msec
Minimum Pulse Length	2 μs

Receivers of the Legacy Arecibo Telescope

The Arecibo Observatory had receivers which spanned in frequency from High Frequency (HF) to X-band, the parameters of which are shown in Table 12. These receivers could be used as the receive antenna for a bistatic radar configuration. An experiment using a radio telescope as a receiver in a bistatic system for the detection of orbital debris was performed in 1997 (Leushacke, Mehrholz, & Jehn, 1997) using the Tracking and Imaging Radar (TIRA) operated by the Research Establishment for Applied Science, commonly referred to as FGAN, and the Effelsburg Radio Telescope operated by the Max Plank Institute for Radio Astronomy.

TIRA is a 34 m L-band monopulse radar which is located 21 km from the 100 m diameter Effelsburg Radio Telescope. In the experiment, named COBEAM-1/96, the dishes were pointed to intersect at an altitude of 850 km with an altitude window that ranged from 750 km to 980 km. During the 24-hour observation, 317 objects were detected yielding a detection rate of 13.02 per hour. The minimum detectable size at Effelsburg was approximately 1 cm using 32 integrated

pulses. This is a factor of two improvement over the TIRA monostatic limit of 2 cm at 1000 km using 64 integrated pulses. One of the main drawbacks of COBEAM-1/96 was Effelsburg's lack of a monopulse receiver. This meant that the authors could not correct for the off-boresight attenuation and could only report a minimum possible size of the debris.

Improved debris observation campaigns were performed in 2006 and 2007 (Ruiz, Leushacke, Jehn, & Keller, 2006) using TIRA and a multi-beam receiver at the Effelsburg Radio Telescope, a receiver similar to that of the ALFA multi-beam receiver of the LAT. The experiments, MBPE-1/06 and MBPE-1/07, had minimum detectable sizes similar to that of COBEAM-1/96. Using algorithms for path estimation through multi-beam receivers (Ruiz, Leushacke, & Rosebrock, 2005) they were able to produce path estimates for objects as small as 3.55 cm at 1390 km (Letsch, et al., 2009).

Numerous other radio telescopes have also been proposed for the study of orbital debris. A proposal to use the Sardinian Radio Telescope in this regard was made in 2005 (Saba, et al., 2005). A sensor pair dubbed the Bistatic Radar for LEO Tracking (BIRALET) used the Sardinian Radio Telescope and the Flight Termination System (FTS) of the Italian Joint Test Range of Salto di Quirra to perform observations of cataloged objects in 2017 (Muntoni, et al., 2017). Another system, Bistatic Radar for LEO Survey (BIRALES), proposed using the FTS and the multi-beam Northern Cross Radio Telescope and performed simulated observations of cataloged objects in 2014 (Morselli, et al., 2014). Several papers describing experiments using the Evpatoria RT-70 transmitter and the Medicina Radio Telescope have also been published. One paper in 2001 (Zaitsev, Ignatov, di Martino, Montebugnoli, & Nabatov, 2001) proposed the measurement of centimeter sized objects in the geostationary ring. Observations performed in 2008 (Pupillo, et al.,

2008) indicate that the Medicina-Evpatoria pair has the potential to observe centimetric to sub-centimetric debris in LEO.

Table 12. Receivers of the LAT. (NAIC, 2021)

Name	Frequency Range (GHz)	Native Polarization	Gain (K/Jy)	Temp. (K)	Beam Size (arcmin)
CH 47 - MHz	***	Dual Circular	***	***	110x94
327 - MHz	0.312 - 0.342	Dual Linear	11	113	15x14
CH 430 - MHz	0.425 - 0.435	Dual Circular	20	120	9.5x8.5
430 - MHz	0.422 - 0.442	Dual Circular	11	50	12x10
ALFA	1.225-1.525	Dual Linear	10	30	3.8x3.3
L-wide	1.15 - 1.73	Dual Linear	10	33	3.5x3.1
S-low	1.8 - 3.1	Dual Linear	8	40	2.0x1.8
S-narrow	2.33 - 2.43	Dual Circular	10	25	2.0x1.8

Next Generation Arecibo Telescope

On 1 December 2020 the LAT unexpectedly collapsed. In its 57 years, the LAT's unique capabilities contributed significantly to three separate major scientific areas: planetary science, space and atmospheric sciences, and astronomy. In the wake of the collapse, a team of scientists and engineers have begun to envision the future of the Arecibo Observatory. A white paper was released describing the concept for the NGAT which features a larger frequency coverage, higher gain, more transmit power, and a greater field of view, among other improvements (Roshi, et al., 2021).

To meet the science requirements of large sky coverage, large collection area, excellent surface brightness sensitivity, and several megawatts of transmitting power, a 'compact dish array

on a single plane' design was chosen. Two variations of the design are an array of 1,112 dishes of 9 m in diameter within a 314 m diameter circle and an array of 400 dishes of 15 m diameter within a 331 m diameter circle. It is also proposed that the signals from each dish be digitized as near to the receiver as possible, with the suggestion that spatial Radio Frequency nulling and grating lobe suppression could be performed with proper element weighting. The estimated gain and transmit power of the NGAT at UHF, S-band, and C-band are shown in Table 13.

Table 13. Estimated gain and transmit power of the NGAT.

	UHF	S-band	C-band
Frequency	430 MHz	2380 MHz	5000 MHz
Gain	61.5 dB (20 K/Jy)	76.4 dB (20 K/Jy)	82.4 dB (18 K/Jy)
Transmit Power	10 MW	5 MW	5 MW

Performance Metrics

There are various bistatic and monostatic configurations in which the LAT and NGAT could be used for orbital debris measurement. As previously stated, two key performance metrics for evaluating the utility of any particular configuration are the minimum detectable debris size and the total debris detection rate. The description of these parameters and their method of calculation are briefly recapitulated. Detailed mathematical derivations were presented in Chapters Two and Three.

Radar does not directly measure the size of an object, but rather measures an object's RCS. An object’s RCS depends not only on size, but on the reflectivity of its surface and the directivity of the radar reflection caused by the target's shape. To relate RCS to size the NASA SEM is used. This model creates a one-to-one mapping of RCS to size for radar measurements of orbital debris. Knowing the transmitter and receiver properties of a radar, one can use the bistatic radar equation along with a choice of signal-to-noise (SNR) threshold to estimate a minimum detectable RCS.

This is then related to a minimum detectable size via the NASA SEM. Since minimum detectable RCS and size are altitude dependent, these parameters are presented at a standard altitude of 1000 km.

Estimates of total debris detection rate are important considering even with an excellent minimum detectable size, one must be able to obtain statistically significant data in a reasonable amount of time. While minimum detectable size mostly depends on the radar sensitivity, the total debris detection rate also depends on the geometry of the beam intersection and the actual flux of debris on orbit. To estimate debris flux, NASA's ORDEM is used. ORDEM can be used in "Telescope Mode" to estimate debris flux as a function of size and altitude using a radar's location and pointing direction. This is then translated to a "detectable" debris flux through the calculation of a probability of detection as a function of size and altitude, interpreted as the fraction of debris detected of each size at each altitude. This detectable debris flux is then multiplied by the altitude dependent beam intersection area of the radar to calculate a total count rate of detectable debris. Here the total debris detection rate is integrated from 400 km to 2000 km altitude for each instrument.

Detection Rate and Minimum Detectable Size Estimates for the LAT and NGAT

Monostatic Configurations

The UHF radar was the only LAT configuration that could act monostatically for debris detection. The ideal operating characteristics of the transmitter are detailed in Table 11. Table 14 shows that in this configuration the LAT could detect objects as small as 1.4 cm at 1000 km altitude, while the NGAT could detect objects as small as 9.3 mm. While not as sensitive as HUSIR, these configurations would still be among the most sensitive instruments used for these kinds of measurements, while also measuring an under-samples range of orbital inclinations. Additionally, there exists the opportunity to perform commensal observations with existing

ionospheric measurements. In (Zhou, Tepley, & Sulzer, 1995) the echoes from meteor ablation trails between 80 km and 120 km altitude that were considered "noise" in the ionospheric measurements turned out to be a fortuitous source of meteor observations. Methods were developed in (Wen, Doherty, Mathews, & Janches, 2005) to filter meteors from the ionospheric data to "clean" the data and produce a commensal meteor detection data set. Similar techniques can be developed for the detection of orbital debris at higher altitudes providing useful data with little additional overhead.

Several data sets taken with the LAT already exist and are available from the Arecibo Observatory Data Archive. Even without new observations from the NGAT, there exists the opportunity to extract useful orbital debris data from the instruments of the Arecibo Observatory.

Table 14. Predicted UHF Monostatic Performance.

	LAT: UHF	NGAT: UHF
Minimum RCS @ 1000 km	-75.94 dBsm	-87.26 dBsm
Minimum Size @ 1000 km	14.4 mm	9.30 mm
Intersection Area	14166.65 km^2	14166.65 km^2
Total Count Rate	3.66 per hour	7.76 per hour

Configurations with the VLBI Reference Antenna

The Arecibo Observatory has a 12 m antenna located approximately 450 m North of the center of the main dish. The antenna was built to act as a reference antenna for calibration when the LAT's main dish was used for Very Long Baseline Interferometry (VLBI). The characteristics of the VLBI reference antenna are summarized in Table 15. Since the antenna is so close to the main dish and the receiver beam width is comparatively large, the beams nearly entirely overlap. This could be described as a quasi-monostatic configuration. Assuming a 3 msec CW pulse, in this configuration the LAT could detect an 8 mm object at 1000 km altitude, as shown in Table 16. Although the minimum detectable RCS is higher than that of the UHF monostatic configuration,

the minimum detectable size is smaller because of the increased RCS to size "efficiency" of S-band as compared to UHF in the Rayleigh scattering regime.

Using the NGAT at S-band would allow the detection of debris as small as 5.5 mm at 1000 km altitude, roughly the same sensitivity as HUSIR. The VLBI reference antenna does not currently have a C-band receiver. However, if one with similar noise and gain parameters were to be installed, a minimum detectable size of 2.6 mm at 1000 km with a total count rate of 63 hits per hour would be achievable. This level of performance is comparable to the Goldstone Orbital Debris Radar, the most sensitive radar currently used for orbital debris measurements in LEO.

The Goldstone Orbital Debris Radar is a bistatic radar which used DSS-14 as a transmitter and DSS-15 as a receiver until it was decommissioned in 2018 (Murray, 2019). While new Goldstone configurations with a comparable sensitivity have been employed, the instantaneous altitude coverage for a given intersection altitude was greatly reduced due to the increased bistatic baseline. Since this configuration of the NGAT can view all LEO altitudes simultaneously, it could recreate the performance of the legacy Goldstone system.

Table 15. VLBI Receiver Parameters. (Perilat, 2021)

Frequency	2380 MHz
Gain	47.2 dB (0.024 K/Jy)
T_{sys}	107 K
HPBW	0.665°
Coordinates	18 ° 20'53.9" N, 66° 45'5.7" W

Table 16. Predicted VLBI Performance.

	LAT: S-band	NGAT: S-band	NGAT: C-band
Minimum RCS @ 1000 km	-61.45 dBsm	-71.14 dBsm	-77.69 dBsm
Minimum Size @ 1000 km	8.00 mm	5.51 mm	2.61 mm
Intersection Area	3509.88 km^2	3509.88 km^2	1668.72 km^2
Total Count Rate	2.23 per hour	6.14 per hour	63.14 per hour

Configurations with the VLBA Antenna St. Croix

On St. Croix in the Virgin Islands there is an antenna that is part of the Very Long Baseline Array (VLBA). It is located 238 km South-West of the Arecibo Observatory. As indicated in Table 17, the dish has a larger aperture and lower system temperature than the 12 m antenna on site. Table 18 shows that in this configuration at S-band the LAT could detect a 5.5 mm object at 1000 km altitude, while the NGAT could detect a 3.8 mm object. The altitude coverage from beam-null to beam-null at 1000 km is approximately 56 km. Even with the small intersection area, this configuration would manage a detection rate of 0.4 per hour.

At C-band, it would be possible to detect objects with sizes down to 1.7 mm. Even though the intersection area is small, debris flux increases rapidly below 3 mm resulting in a reasonable detection rate of 4.4 per hour. Although multiple pointings would be required for a full survey of LEO, the sensitivity afforded by this bistatic arrangement would provide unprecedented terrestrial radar data of the debris environment.

Table 17. VLBA Receiver Parameters. (Romney, 2019)

Frequency	2380 MHz / 5000 MHz
Gain	52.7 dB / 60.6 dB (0.087 K/Jy / 0.119 K/Jy)
T_{sys}	40 K
HPBW	0.352° / .074°
Coordinates	17° 45'23.5 N, 64° 35'1.5" W

Table 18. Predicted VLBA Performance.

	LAT: S-band	**NGAT: S-band**	**NGAT: C-band**
Minimum RCS @ 1000 km	-70.87 dBsm	-80.57 dBsm	-88.54 dBsm
Minimum Size @ 1000 km	5.57 mm	3.84 mm	1.72 mm
Intersection Area	47.25 km^2	47.25 km^2	10.70 km^2
Total Count Rate	0.10 per hour	0.40 per hour	4.44 per hour

Configurations with the Green Bank Radio Telescope

The Green Bank Radio Telescope (GBT) is located in Green Bank, West Virginia. It is the largest fully steerable radio telescope in the world and has the lowest system temperature of all receivers mentioned in this paper. The receiver parameters of the GBT at S-band and C-band are given in Table 19.

As shown in Table 20, in this configuration the LAT could detect a 4.0 mm object at 1000 km, making it more sensitive than HUSIR. At S-band the NGAT could detect objects as small as 2.8 mm. At C-band the NGAT would be able to detect objects down to 1.3 mm, the smallest size yet. Although great for sensitivity, the large aperture and correspondingly narrow beam of the GBT as well as the large geographic separation drastically reduces the intersection area. The altitude coverage of this configuration from beam-null to beam-null at 1000 km is approximately 10 km at S-band. At C-band, the altitude coverage is too small (more narrow than the altitude bins of ORDEM output) to allow for an accurate estimation of total count rate. Due to the diminished instantaneous altitude coverage, this configuration would be more useful to perform targeted follow-up observations of an on-orbit breakup. Additionally, due to the elevation limits of the GBT, only altitudes above 800 km could be observed.

Table 19. GBT Receiver Parameters. (GBT Scientific Staff, 2021)

Frequency	2380 MHz / 5000 MHz
Gain	66.4 dB / 72.9 dB (2.0 K/Jy)
T_{sys}	18 K / 18 K
HPBW	5.8 arcmin / 1.2 arcmin
Coordinates	38° 25' 59.2" N, 79° 50'23.4" W

Table 20. Predicted GBT Performance.

	LAT: S-band	NGAT: S-band	NGAT: C-band
Minimum RCS @ 1000 km	-79.5 dBsm	-89.19 dBsm	-95.79 dBsm
Minimum Size @ 1000 km	4.00 mm	2.76 mm	1.31 mm
Intersection Area	6.87 km^2	6.87 km^2	2.05 km^2
Total Count Rate	0.04 per hour	0.18 per hour	***

NGAT Design Suggestions

While the presented NGAT design has appreciable potential for performing measurements of orbital debris, there are three design suggestions that would significantly improve the performance of the NGAT for statistical sampling of the debris environment in LEO. These are: fast transmit-receive switching enabling monostatic LEO observations, multi-beam receiver capabilities for path through the beam estimation, and a high dynamic range receiver for the measurement of debris over orders of magnitude in size.

Fast transmit-receive switching would allow for monostatic observations of LEO at S- and C-band frequencies. This would maximize sensitivity by using the superb gain of the NGAT on reception as well as transmission. In order to measure debris at 400 km altitude, the nominal orbit altitude of the ISS, the NGAT would need to start receiving echoes at approximately 2.7 msec from the leading edge of the pulse. If the HUSIR debris waveform is copied with a pulse length of 1.6384 msec, the necessary switching time is approximately 1 msec. This is not possible by physically rotating the transmitter and receiver in and out of the focus as was done with the LAT Planetary Radar. Some form of electronic switching or circulator circuit would be necessary, which would unfortunately reduce isolation and raise the system temperature. However, even assuming a pulse length and system temperature similar to HUSIR, the NGAT would still be capable of detecting millimeter-sized objects at 1000 km altitude, as will be shown in later sections.

In statistical LEO debris observations, like the ones discussed thus far, the radar points in a single direction and measures objects as they pass through the radar beam. Since the objects fly randomly through the beam, not necessarily through the antenna boresight, knowledge of the path taken by the object through the beam can be used to correct for off-axis beam shape losses to obtain a more accurate integrated RCS measurement. Knowledge of the path through the beam can also be used to estimate the orbital inclination of the debris. HUSIR performs this path through the beam estimation using information from the difference channels of a monopulse receiver. A monopulse receiver provides an angular offset measurement for each pulse using the differences between four or more squinted beams from the receiver horn. Methods for path through the beam estimation with multi-beam receivers in a bistatic radar system have been discussed in (Ruiz, Leushacke, & Rosebrock, 2005), (Ruiz, Leushacke, Jehn, & Keller, 2006), (Letsch, et al., 2009), and (Morselli, et al., 2014). To use similar techniques, the NGAT would need to provide a minimum of four receive beams to perform similar path through the beam estimates.

One final important aspect is the dynamic range of the receiver. While the majority of debris objects coming through the radar beam would be small, occasionally large objects may pass through the beam, causing the receiver to saturate and result in an underestimate of the debris object's true size. In particular, orbital debris data from the Goldstone Orbital Debris Radar has shown that limited dynamic range affects the measurement of large debris, effectively limiting Goldstone's practical measured size distributions to smaller than 1 cm (Murray, Miller, Matney, Anz-Meador, & Kennedy, 2019). HUSIR increases its dynamic range through the use of an automatic gain control (AGC) unit. When a signal begins to saturate the receiver, attenuation is applied to the receive signal automatically to prevent further saturation of the front-end receivers. This allows HUSIR to measure objects as small as approximately 5 mm at 1000 km to as large as

several meters. While some form of AGC would be ideal, it is only necessary that the receiver have enough dynamic range to measure large enough objects to overlap with existing data sources.

For radar, one defines dynamic range as the ratio of maximum signal power for which the receiver is not saturated to the minimum signal power for which the receiver still detects something. This corresponds to the largest object at the lowest altitude and the smallest object at the highest altitude, or

$$D = \frac{P_{max}}{P_{min}} = \frac{\sigma_{max} R_{max}^4}{\sigma_{min} R_{min}^4} . \quad (16)$$

One can invert the NASA SEM to determine the corresponding RCS at a size of interest. For excellent overlap, one would want to measure from roughly 1 mm to 10 cm in size. Coverage from 1 mm to 1 cm would give similar large size overlap as the Goldstone Orbital Debris Radar. Coverage from 1 mm to 5.5 mm would be about the minimum size range necessary to overlap with HUSIR data. Assuming measurements from 400 km to 1000 km with no distortion is desired, each of these size ranges (1 mm to 10 cm, 1 mm to 1 cm, and 1 mm to 5.5 mm) would require 111 dB, 76 dB, and 60 dB of dynamic range, respectively.

Detection Rate and Minimum Detectable Size Estimates for a Monostatic NGAT

While the anticipated increases to both gain and transmission power do improve performance for the bistatic configurations outlined in the preceding sections, the estimation of monostatic performance is still of interest. The current design of the NGAT still does not allow for monostatic operation of the planetary radar for LEO observations. It is mentioned in the NGAT white paper that the addition of fast transmit-receive switching to the planetary radar would allow for the measurement of millimeter-sized orbital debris in LEO. Here these claims are verified and quantified by calculating minimum detectable sizes and debris detection rates, assuming monostatic operation with a 1.6384 msec transmit pulse, such as that used by HUSIR.

If the NGAT could incorporate fast switching, its superior gain could be leveraged on reception as well as transmission, significantly increasing its sensitivity for LEO debris measurements. Since this kind of switch would likely increase the system temperature of the receiver, a similar system temperature as that of HUSIR is assumed for these calculations; 186 K. With this assumption, the NGAT could detect objects as small as approximately 2 mm at S-band, as show in Table 21. This is even smaller at C-band, approximately 1 mm, which completely bridges the gap between on-orbit and terrestrial LEO debris measurements. Because the modeled flux increases significantly between 1 cm and 1 mm, the predicted count rate is approximately 6.6 detections per minute at S-band and 1.1 detections per second at C-band.

Table 21. NGAT Monostatic Performance: S-band and C-band.

	NGAT: S-band	NGAT: C-band
Minimum RCS @ 1000 km	-95.15 dBsm	-100.77 dBsm
Minimum Size @ 1000 km	2.19 mm	1.08 mm
Intersection Area	2559.43 km^2	1218.29 km^2
Total Count Rate	394.03 per hour	3973.17 per hour

Chapter Summary

There exist gaps in the empirical knowledge of the debris environment; millimetric debris in LEO, low inclination debris in LEO, and centimetric debris in GEO. In this Chapter, key debris observation parameters were described; minimum detectable RCS, minimum detectable size, observational surface area for bistatic radar, and total debris detection rates. These observation parameters were estimated for the LAT and NGAT and compared to the performance of the HUSIR radar.

It has been demonstrated that the LAT and NGAT could be used to fill many gaps of empirical knowledge of the debris environment. The location of the Arecibo Observatory would provide access to 27% more orbital inclinations than HUSIR. There exists data from the LAT in

the Arecibo Observatory Data Archive from which useful measurements of centimeter-sized debris at low inclinations can be extracted. The NGAT could also gather significant amounts of data on centimeter-sized debris through commensal observations. One NGAT bistatic arrangement could have a sensitivity comparable to the Goldstone Orbital Debris Radar while observing at all LEO altitudes in a single pointing. Another bistatic arrangement could provide measurements of debris as small as 1.7 mm.

Three design suggestions that would significantly improve the performance of the NGAT for statistical sampling of the debris environment in LEO were presented; fast transmit-receive switching enabling monostatic LEO observations, multi-beam receiver capabilities for path through the beam estimation, and a high-dynamic range receiver for the measurement of debris over orders of magnitude in size. With the proposed design suggestions, the NGAT could detect objects as small as 1 mm at 1000 km. This would completely bridge the gap between on-orbit *in-situ* debris measurements and terrestrial radar debris measurements.

Ultimately, it has been shown that data from the LAT and NGAT can be used significantly improve short-term debris environment models which are used to inform spacecraft design and operations ultimately reduce the potential risk to space operations.

CHAPTER FIVE:

SUMMARY AND FUTURE WORK

Summary

Orbital debris has been around since the dawn of the space age. It is unique because it presents a man-made risk to space operations in Earth orbit, one that has surpassed the natural risk posed by micrometeoroids in LEO. The density of debris on orbit has already passed the critical density, after which the population will continue to grow unless remediation measures are implemented. This makes the pervasive risk posed by orbital debris all the more important to characterize. Data deficiencies in key size regimes in LEO still exists. These happen to coincide with the size regimes that pose the greatest mission-ending risk to spacecraft in LEO. The Arecibo Observatory as a potential data source was identified and the necessary tools to evaluate its efficacy for debris measurements in LEO were developed. The Arecibo Observatory, particularly the proposed NGAT, has the potential to close the critical size gap between 1 mm and 3 mm for debris measurements in LEO.

In Chapter One, an introduction to orbital debris describing the sources, orbital lifetimes, and quantities of debris on orbit was given. Future predicted growth of the environment and its implications on mitigation and remediation were discussed. The threat posed by orbital debris to spacecraft was illustrated. The response approach taken by the NASA ODPO to the orbital debris problem was presented, including descriptions of the various models and measurement approaches used to inform the development of debris mitigation practices, spacecraft design standards, and space policy development. A deficiency data sources for debris between 1 mm and 3 mm in LEO was identified and its implications emphasized. Bistatic radar measurements including radio

telescopes, particularly the Arecibo Observatory, were suggested as a potential source of data to bridge the crucial size gap.

In Chapter Two, a novel method to calculate the lateral surface area for a bistatic radar beam overlap was developed. An existing monostatic algorithm was presented and compared to the bistatic approach. Comparisons of the monostatic case showed the new bistatic method converges to that of the monostatic method in the monostatic case. A case study of this method applied to an existing bistatic radar system was presented. Finally, a general guide was developed for total error versus baseline and target altitude. This guide allows users to determine when the bistatic area calculation is necessary, based on the error tolerance of the application.

In Chapter Three, two key observation parameters for debris were identified: minimum detectable size and total count rate. Methods for estimating these parameters were developed. A report describing measurements performed by HUSIR was presented including radar parameters, detection methodology, and results. These results were then compared to predictions made using the developed methods and shown to be in good agreement.

Finally, in Chapter Four the Arecibo Observatory and its array of transmitters and receivers were presented. The collapse of the LAT and the capabilities of the proposed NGAT were discussed. A survey of measurements performed by the LAT and other radio telescopes of orbital debris and micrometeors was given. Performance of the LAT and NGAT in various bistatic and monostatic radar configurations was estimated. Design changes that would significantly improve the performance of the NGAT for statistical LEO debris measurements were suggested. Finally, it was shown that, with the suggested improvements, the NGAT could bridge the size gap of measurement data in LEO and significantly improve orbital debris models in the size regime that poses the highest mission-ending risk to spacecraft in LEO.

Future Work

Unfortunately, since the LAT is no longer operational and the NGAT is not yet built, observations like the ones proposed are not currently possible. However, this dissertation can serve as incentive to develop the necessary equipment for the NGAT to perform these observations at peak potential when the NGAT becomes operational. Once the NGAT is operational, proof of concept observations will be the top priority.

In the interim, one future work topic involves developing methods to analyze existing LAT radar measurements for the presence of orbital debris signatures. In Chapter Four, it was shown that the UHF radar used for incoherent scatter measurements of the ionosphere would have the capability to measure the centimeter-sized debris population in LEO. In particular, these observations would provide measurements of an unmeasured population of centimeter-sized low-inclination debris. There exists the opportunity to perform commensal observations with existing ionospheric measurements. A precedent for this already exists. Meteor ablation trails were causing "noise" in ionospheric measurements between 80 km and 120 km altitude and turned out to be a fortuitous source of meteor observations. The Arecibo Observatory Data Archive contains several existing data sets taken with the LAT. These datasets represent an opportunity to extract useful orbital debris data from the instruments of the Arecibo Observatory, even without new observations from the NGAT.

Another future work topic would investigate the ability of Arecibo to perform observations of debris in GEO and cislunar orbital regimes. Although the probability of a damaging impact in GEO is less than in LEO, it is still important to understand the GEO debris environment because geostationary orbits are a valuable limited resource that need to be preserved, GEO orbital lifetimes

are extremely long, and many high value spacecraft already inhabit GEO. The nominal size limit for tracked debris in GEO is approximately 1 m. One of the functions of NASA's ES-MCAT telescope is to perform GEO debris surveys. It is estimated to be able to detect objects down to approximately 13 cm in GEO (Lederer, Stansbery, Cowardin, Kervin, & Hickson, 2013). As previously mentioned, the Evpatoria RT-70 transmitter and the Medicina Radio Telescope bistatic radar has been suggested to perform measurements of centimeter sized debris in GEO. It has also been suggested that Arecibo can be used in a similar capacity (Taylor & Rivera-Valentín, 2019) (Roshi, et al., 2021). Orbital debris in cislunar space is a relatively new topic of interest (Boone, 2021) (Guardabasso, Lizy-Destrez, & Ansart, 2021) (Holzinger, Chow, & Garretson, 2021). It is of particular interest to get ahead of this problem using lessons learned from the development of mitigation practices for LEO and GEO orbits with the advent of NASA's Artemis program which aims to use lunar and cislunar space extensively in the near future. The potential of the NGAT to perform measurements of debris in GEO and cislunar space should be evaluated.

A third future work topic would involve identifying previously unexamined radar assets and applying the methods developed here to estimate their performance. A prime candidate is the new GBT planetary radar. A proposal to add a high-powered Ka-band transmitter to the GBT was presented in 2020 (Bonsall, et al., 2020). The proposal features a center frequency of 35 GHz with a peak power of 500 kW. It will also have a monopulse receiver, which could be used to determine the path through the beam taken by a piece of debris, like is done with HUSIR. Combining a high transmit power with the 100 m diameter dish would give the GBT the potential for the measurement of incredibly small debris in LEO. Since the beam will be very narrow due to the diameter of the dish, the lateral surface area may be too small to observe debris in a reasonable

amount of time. Therefore, it is of interest to evaluate the minimum detectable size and total count rate of the GBT planetary radar.

REFERENCES

Anz-Meador, P., Opiela, J., Shoots, D., & Liou, J.-C. (2018). *History of On-Orbit Satellite Fragmentations, 15th Edition.* Houston: NASA Johnson Space Center.

Anz-Meador, P., Ward, M., Manis, A., Nornoo, K., Dolan, B., Claunch, C., & Rivera, J. (2019). The Space Debris Sensor Experiment. *First International Orbital Debris Conference.*

Balogun, F., Brunetti, A., & Cesareo, R. (2000). Volume of Intersection of Two Cones. *Radiation Physics and Chemistry*.

Barber, C., Dobkin, D., & Huhdanpaa, H. (1996). The Quickhull algorithm for convex hulls. *ACM Trans. on Mathematical Software*. Retrieved from http://www.qhull.org

Barton, D. K., Brillinger, D., El-Shaarawi, A. H., McDaniel, P., Pollock, K. H., & Tuley, M. T. (1998). *Final Report of the Haystack Orbital Debris Data Review Panel.* Houston: NASA Johnson Space Center.

Beyer, W., Fawcett, L., Mauldin, R., & Swartz, B. (1987). The Volume Common to Two Congruent Circular Cones whose Axes Intersect Symmetrically. *Journal of Symbolic Computation*.

Bohannon, G., Caampued, T., & Young, N. (1994). *First Order RCS Statistics of Hypervelocity Impact Fragments.* XonTech Report 940128-BE-2305.

Bonsall, A., Watts, G., Lazio, J., Taylor, P., Rivera-Valentin, E., Howell, E., . . . Whitten, J. (2020). GBT Planetary Radar System. *Astro2020 APC White Paper.*

Boone, N. R. (2021). Cislunar Debris Propagation Following a Catastrophic Spacecraft Mishap. Retrieved from Theses and Dissertations: https://scholar.afit.edu/etd/4971

Briczinski, S. J., Mathews, J. D., & Meisel, D. D. (2009). Statistical and fragmentation properties of the micrometeoroid flux observed at Arecibo. *Journal of Geophysical Research: Space Physics, 114*(A4).

Brogan, C., & Hunter, T. (2014). *ALMA Single Dish Imaging Parameters, a Comparison of Observed Beams to Predicted Beams, and a Demonstration of the Method for Measuring Jy/K.* NRAO Atacama Large Millimeter Array.

Christiansen, E., & Lear, D. (2012). *Micrometeoroid and Orbital Debris Environment & Hypervelocity Shields.* Houston: NASA Johnson Space Center.

Cowardin, H., Lederer, S., Stansbery, G., Seitzer, P., Buckalew, B., Abercromby, K., & Barker, E. (2014). NASA's Optical Measurement Program 2014. *Proceedings of the AMOS 2014 Technical Conference.* Maui.

Dalquist, C., & Bohannon, G. (1991). *Physical Descriptions of Debris Objects Used in Static RCS Measurements.* XonTech Report 910555-1978.

European Space Agency. (2021). *ESA's Annual Space Environment Report.* Darmstadt: ESA European Space Operations Centre.

Everett, R., Caampued, T., & Chu, J. (1991). *Summary of Data Processing of September 1990 SPC Debris Data.* XonTech Report 910147-1937.

Everett, R., Dalquist, C., & Caampued, T. (1991). *Summary of Processing of January 1991 SPC Debris Data.* XonTech Report 9100393-1965.

Folkner, W. (2018). *DSN Coverage and Geometry.* NASA Jet Propulsion Laboratory DSN Handbook.

Foster, J. L., Stansbery, E., Matney, M. J., Benbrook, J. R., & Jarvis, K. S. (2003). *Haystack and HAX Radar Measurements of the Orbital Debris Environment; 1999-2002.* Houston: NASA Johnson Space Center.

Fritsch, F. N., & Butland, J. (1984). A method for constructing local monotone piecewise cubic interpolants. *SIAM Journal on Scientific and Statistical Computing, 5*(2), 300-304.

GBT Scientific Staff. (2021). *Observing with the Green Bank Telescope.* Green Bank Observatory. Retrieved from https://www.gb.nrao.edu/scienceDocs/GBTog.pdf

Goldstein, R., & Goldstein, S. (1995). Flux of Millimetric Space Debris. *The Astronomical Journal, 110*(3). doi:10.1086/117612

Goldstein, R., & Randolph, L. (1992). Rings of Earth. *IEEE Transactions on Microwave Theory and Techniques, 40*(6), 1077-1080. doi:10.1109/22.141338

Goldstein, R., Goldstein, S., & Kessler, D. (1998). Radar observations of space debris. *Planetary and Space Science, 46*(8), 1007-1013. doi:10.1016/S0032-0633(98)00026-9

Guardabasso, P., Lizy-Destrez, S., & Ansart, M. (2021). Lunar Orbital Debris Mitigation: Characterization of the Environment and Identification of Disposal Strategies. *8th European Conference on Space Debris.*

Holzinger, M., C. C., & Garretson, P. (2021). *A Primer on Cislunar Space.* Air Force Research Laboratory.

Horstman, M., Papanyan, V., Juarez, Q., & Hamilton, J. (2014). *Haystack and HAX Radar Measurements of the Orbital Debris Environment: 2006-2012.* Houston: NASA Johnson Space Center.

Hubbell, J. (1965). Common Volume of Two Intersecting Cylinders. *Journal of Research of the National Bureau of Standards, Section C: Engineering and Instrumentation*.

Hughes, R., & Clamons, J. (1974). *Volume Intersection of Two Identical Right Circular Cones.* NRL Memorandum Report 2811.

Hyper Velocity Impact Technology. (2021). *Impact Images*. Retrieved from https://hvit.jsc.nasa.gov/impact-images/space-shuttle.cfm

Janches, D., Mathews, J., Meisel, D., & Zhou, Q.-H. (2000). Micrometeor Observations Using the Arecibo 430 MHz Radar: I. Determination of the Ballistic Parameter from Measured Doppler Velocity and Deceleration Results. *Icarus, 145*(1), 53-63.

Kennedy, T., Murray, J., & Miller, R. (2020). Recent Radar Observations of the Sub-Centimeter Orbital Debris Population. *2nd IAA Conference on Space Situational Awareness (ICSSA).*

Kesseler, D., & Cour-Palais, B. (1978). Collision frequency of artificial satellites: The creation of a debris belt. *Journal of Geophysical Research, 83*(A6), 2637-2646. doi:doi:10.1029/JA083iA06p02637

Krisko, P. (2014). The new NASA orbital debris engineering model ORDEM 3.0. *AIAA/AAS Astrodynamics Specialist Conference.*

Lederer, S., Stansbery, E. G., Cowardin, H. M., Kervin, P., & Hickson, P. (2013). The NASA Meter Class Autonomous Telescope: Ascension Island. *Proceedings of the AMOS 2013 Technical Conference.* Maui.

Lee, C. G., Slade, M. A., Jao, J. S., & Rodriguez-Alvarez, N. (2020). Micro-meteoroid and orbital debris radar from Goldstone radar observations. *Journal of Space Safety Engineering, 7*(3), 242-248.

Letsch, R., Leushacke, L., Rosebrock, J., Jehn, R., Krag, H., & Keller, R. (2009). First Results from the Multibeam Bistatic Beampark Experiment at FGAN. *5th European Conference on Space Debrs.*

Leushacke, L., Mehrholz, D., & Jehn, R. (1997). First FGAN/MPIfR cooperative debris observation campaign: experiment outline and first results. *2nd European Conference on Space Debris.* Darmstadt.

Liou, J., Hall, D., Krisko, P., & Opiela, J. (2004). LEGEND - a three-dimensional LEO-to-GEO debris evolutionary model. *Advances in Space Research, 34*, 981-986.

Liou, J.-C. (2020). Risk From Orbital Debris and Space Situational Awareness. *2nd IAA Conference on Space Situational Awareness.*

Liou, J.-C., & Johnson, N. (2008). Instability of the present LEO satellite populations. *Advances in Space Research, 41*, 1046-1053. doi:10.1016/j.asr.2007.04.081

Liou, J.-C., Burchell, M., Corsaro, R., Drolshagen, G., Giovane, F., Pisacane, V., & Stansbery, E. (2009). In Situ Measurement Activities at the NASA Orbital Debris Program Office. *5th European Conference on Space Debris.*

Liou, J.-C., Clark, S., Fitz-coy, N., Huynh, T., Opiela, J., Polk, M., . . . Werremeyer, M. (2013). DebriSat- A Planned Laboratory-Based Satellite Impact Experiment for Breakup Fragment Characterization. *6th European Conference on Space Debris.*

Matney, M. (2000). *An Introduction to the Satellite Breakup Risk Assesment Model (SBRAM).* Lockheed Martin Space Operations Company.

Matney, M., Goldstein, R., Kessler, D., & Stansbery, E. (1999). Recent results from goldstone orbital debris radar. *Advances in Space Research*.

McKnight, D., Johnson, N. L., Fudge, M. L., & Maclay, T. D. (1995). *Satellite Orbital Debris Characterization Impact Test (SOCIT) Series Data Collection Report.* Kaman Sciences Corporation.

Miller, R., Murray, J., & Kennedy, T. (2021a). Goldstone Orbital Debris Radar: A Historical Review from a Decade of Observations (2007-2017). *Orbital Debris Quarterly News*, pp. 3-6.

Miller, R., Murray, J., & Kennedy, T. (2021b). *Goldstone Radar Measurements of the Orbital Debris Environment: 2018.* Houston: NASA Johnson Space Center.

Morselli, A., Armellin, R., Di Lizia, P., Bernelli-Zazzera, F., Salerno, E., Bianchi, G., . . . Adami, K. Z. (2014). Orbit determination of space debris using a bi-static radar configuration with a multiple-beam receiver. *International Astronautical Congress.*

Muntoni, G., Schirru, L., Pisanu, T., Montisci, G., Valente, G., Gaudiomonte, F., . . . Fanti, A. (2017). Space Debris Detection in Low Earth Orbit with the Sardinia Radio Telescope. *Electronics*.

Murray, J. (2019). New Geometry for Debris Observations using the Goldstone Orbital Debris Radar. *Orbital Debris Quarterly News, 23*(1 & 2), p. 8.

Murray, J., & Kennedy, T. (2020). *Haystack Ultra-Wideband Satellite Imaging Radar Measurements of the Orbital Debris Environment: 2018.* Houston: NASA Johnson Space Center.

Murray, J., & Kennedy, T. (2021). *Haystack Ultra-Wideband Satellite Imaging Radar Measurements of the Orbital Debris Environment: 2019.* Houston: NASA Johnson Space Center.

Murray, J., Blackwell, C., Gaynor, J., & Kennedy, T. (2019). *Haystack Ultra-Wideband Satellite Imaging Radar Measurements of the Orbital Debris Environment: 2014-2017.* Houston: NASA Johnson Space Center.

Murray, J., Cowardin, H., Liou, J.-C., Sorge, M., Fitz-Coy, N., & Huynh, T. (2019). Analysis of the DebriSat Fragments and Comparison to the NASA Standard Satellite Breakup Model. *First International Orbital Debris Conference.*

Murray, J., Miller, R., Matney, M., & Kennedy, T. (2019). Orbital Debris Radar Measurements from the Haystack Ultra-wideband Satellite Imaging Radar (HUSIR): 2014 – 2017. *First International Orbital Debris Conference.*

Murray, J., Miller, R., Matney, M., Anz-Meador, P., & Kennedy, T. (2019). Recent Results from the Goldstone Orbital Debris Radar: 2016-2017. *First International Orbital Debris Conference.*

NAIC. (2021). *Arecibo Observatory Receivers*. Retrieved from http://www.naic.edu/~astro/RXstatus/rcvrtabz.shtml

NASA. (2008). *Handbook for Limiting Orbital Debris.* Washington, DC: NASA.

National Research Council. (1998). *Protecting the Space Shuttle from Meteoroids and Orbital Debris.* National Academies Press.

Orbital Debris Program Office. (2021a). *Frequently Asked Questions*. Retrieved from https://orbitaldebris.jsc.nasa.gov/faq/

Orbital Debris Program Office. (2021b). Monthly Number of Objects in Earth Orbit by Object Type. *Orbital Debris Quarterly News, 25*(1), 10.

Orbital Debris Program Office. (2021c). *Optical Measurements*. Retrieved from https://orbitaldebris.jsc.nasa.gov/measurements/optical.html

Orbital Debris Program Office. (2021d). *Photo Gallery*. Retrieved from https://orbitaldebris.jsc.nasa.gov/photo-gallery/

Perilat, P. (2021). *Patriot 12 meter telescope*. Retrieved from https://www.naic.edu/~phil/hardware/12meter/patriot12meter.html

Pupillo, G., Bartolini, M., Cevolani, G., Di Martino, M., Falkovich, I., Konovalenko, A., . . . Zoni, L. (2008). Space debris observational test with the Medicina-Evpatoria bistatic radar. *Memorie della Societa Astronomica Italiana Supplementi*.

Romney, J. (2019). *Frequency Bands & Performance*. Retrieved from https://science.nrao.edu/facilities/vlba/docs/manuals/oss2019B/bands-perf

Roshi, D. A., Aponte, N., Araya, E., Arce, H., Baker, L. A., Baan, W., . . . Zambrano-Marin, L. F. (2021). *The Future of the Arecibo Observatory: The Next Generation Arecibo Telescope.* Arecibo Observatory.

Ruiz, G., Leushacke, L., & Rosebrock, J. (2005). Algorithms for Multi-Beam Receiver Data Analysis. *4th European Conference on Space Debris.*

Ruiz, G., Leushacke, L., Jehn, R., & Keller, R. (2006). Improved FGAN/MPIFR bi-static debris observation campaign: experiment outline, analysis algorithms and first results. *57th International Astronautical Congress.*

Saba, L., Di Martino, M., Delbo, M., Cellino, A., Montebugnoli, S., Righini, S., . . . Lazzarin, M. (2005). The Sardinian Radio Telescope as Radar for the study of near-Earth Objects and Space Debris. *Memorie della Societa Astronomica Italiana Supplementi*.

Salter, C. (2020). *An Astronomer's Guide to the Arecibo 305-m Telescope.* NAIC. Retrieved from http://www.naic.edu/ao/scientist-user-portal/astronomy/astronomer-guide

Settecerri, T. J., Stansbery, E., & Hebert, T. (1999). *Radar Measurements of the Orbital Debris Environment: Haystack and HAX Radars October 1990 – October 1998.* Houston: NASA Johnson Space Center.

Skolnik, M. I. (1990). *Radar Handbook.* McGraw-Hill.

Space-Track. (2021). *Satellite Catalog*. Retrieved from https://www.space-track.org/#catalog

Squire, M., Cooke, W., Williamsen, J., Kessler, D., Vesely, W., Hull, S., . . . Cornford, S. (2015). *Joint Polar Satellite System (JPSS) Micrometeoroid and Orbital Debris (MMOD) Assessment.* Houston: NASA Johnson Space Center.

Stansbery, E. G., Bohannon, G., Pitts, C. C., Tracy, T., & Stanley, J. F. (1992). *Characterization of the Orbital Debris Environment Using the Haystack Radar.* Houston: NASA Johnson Space Center.

Stokely, C., Foster, J., Stansbery, E., Benbrook, J., & Juarez, Q. (2006). *Haystack and HAX Radar Measurements of the Orbital Debris Environment; 2003.* Houston: NASA Johnson Space Center.

Stokely, C., Stansbery, E., & Goldstein, R. (2009). Debris flux comparisons from the Goldstone Radar, Haystack Radar, and Hax Radar prior, during, and after the last solar maximum. *Advances in Space Research*.

Sulzer, M. (2004). Meteor science from regular incoherent scatter radar ionospheric observations at Arecibo. *Atmospheric Chemistry and Physics Discussions, 4*(1), 805-831.

Taylor, P. A., & Rivera-Valentín, E. G. (2019). Radar characterization of orbital debris with Arecibo Observatory and the Planetary Radar Investigation, Demonstration, and Exploration (PRIDE) Laboratory. *First International Orbital Debris Conference.*

Thompson, T., Goldstein, R., Campbell, D., Stansbery, E., & Potter, A. (1992). Radar detection of centimeter-sized orbital debris: Preliminary Arecibo observations at 12.5-CM wavelength. *Geophysical Research Letters*.

Vavrin, A., Manis, A., Seago, J., Gates, D., Anz-Meador, P., Xu, Y.-L., . . . Matney, M. (2019). *NASA Orbital Debris Engineering Model ORDEM 3.1 – Software Users Guide.* Houston: NASA Johnson Space Center.

Virtanen, P., Gommers, R., Oliphant, T. E., Haberland, M., Reddy, T., Cournapeau, D., . . . SciPy 1.0 Contributors. (2020). SciPy 1.0: fundamental algorithms for scientific computing in Python. *Nat Methods, 17*, 261-272. doi:10.1038/s41592-019-0686-2

Ward, M., & Anz-Meador, P. (2019). MLI Impact Phenomenology Observed on the HST Bay 5 MLI Panel. *First International Orbital Debris Conference.*

Wen, C.-H., Doherty, J., & Mathews, J. (2004). Time–Frequency Radar Processing for Meteor Detection. *IEEE Transactions on Geoscience and Remote Sensing, 42*(3), 501-510.

Wen, C.-H., Doherty, J., & Mathews, J. (2005). Adaptive filtering for the separation of incoherent scatter and meteor signals for Arecibo observation data. *Journal of Atmospheric and Solar-Terrestrial Physics, 67*(13), 1190-1195.

Wen, C.-H., Doherty, J., Mathews, J., & Janches, D. (2005). Meteor detection and non-periodic bursty interference removal for Arecibo data. *Journal of Atmospheric and Solar-Terrestrial Physics, 67*(3), 275-281.

Xu, Y.-l., & Stokely, C. (2005). A Statistical Size Estimation Model for Haystack and HAX Radar Detections. *56th International Astronautical Congress.* Fukuoka.

Zaitsev, A., Ignatov, S., di Martino, M., Montebugnoli, S., & Nabatov, A. (2001). Proposal on centrimetric space debris radar detection in geostationary ring. *3rd European Conference on Space Debris.*

Zhou, Q. H., & Kelley, M. C. (1997). Meteor observations by the Arecibo 430 MHz incoherent scatter radar. II. Results from time-resolved observations. *Journal of Atmospheric and Solar-Terrestrial Physics, 59*(7), 739-752.

Zhou, Q., Tepley, C. A., & Sulzer, M. P. (1995). Meteor observations by the Arecibo 430 MHz incoherent scatter radar-I. Results from time-integrated observations. *Journal of Atmospheric and Terrestrial Physics, 57*(4), 421-431.